

Revisiting the Relationship between the Long GRB Rate and Cosmic Star Formation History Based on a Large Swift Sample

Jing-Meng Hao^{1,2}, Liang Cao^{3,4}, You-Jun Lu^{3,4}, Qing-Bo Chu^{3,4}, Jun-Hui Fan^{1,2}, Ye-Fei Yuan⁵
and Yu-Hai Yuan^{1,2}

ABSTRACT

The exact relationship between the long gamma-ray burst (LGRB) rate and the cosmic star formation rate (CSFR) is essential for using LGRBs as cosmological probes. In this work, we collect a large sample composed of 371 Swift LGRBs with known redshifts and prompt emission properties. We first compare the rest-frame prompt properties of these bursts in different redshift bins, finding negligible redshift evolution of the luminosity of LGRBs with $L_{\text{iso}} \gtrsim 10^{51} \text{ erg s}^{-1}$ between $z \sim 1$ and $z \sim 4$. Then, by utilizing the CSFR obtained from the large-scale cosmological hydrodynamical simulation, the Illustris simulation, we calculate the cumulative redshift distribution of LGRBs under different metallicity thresholds. After comparing with our sample, we find that the predictions with a moderate threshold between $0.3 Z_{\odot} \leq Z_{\text{th}} \leq 1.0 Z_{\odot}$ are consistent with the sample between redshift $0 < z < 3$, while at higher redshifts between $3 < z < 5$, all metallicity thresholds fit the data well. When changing to an empirical model based on observations, the predictions show similar results as well. After comparing with the metallicity distribution of the observed LGRB host galaxies between $0 < z < 1$, we confirm that the production of LGRBs in galaxies with super-solar metallicity is suppressed. Nevertheless, considering that a significant fraction of stars are born in sub-solar metallicity environments at $z \gtrsim 3$, we suggest that, as a first approximation, LGRBs can be used as direct tracers of the CSFR in this redshift range.

Subject headings: Gamma-ray bursts, Star formation, Galaxy chemical evolution

¹Center for Astrophysics, Guangzhou University, Guangzhou 510006, China; jmhao@gzhu.edu.cn

²Astronomy Science and Technology Research Laboratory of Department of Education of Guangdong Province, Guangzhou 510006, China

³National Astronomical Observatories, Chinese Academy of Sciences, 20A Datun Road, Beijing 100101, China

⁴School of Astronomy and Space Sciences, University of Chinese Academy of Sciences, 19A Yuquan Road, Beijing 100049, China

⁵Key Laboratory for Research in Galaxies and Cosmology CAS, Department of Astronomy, University of Science and Technology of China, Hefei, Anhui 230026, China

1. Introduction

Gamma-ray bursts (GRBs) have isotropic luminosities as high as 10^{54} erg s $^{-1}$, making them detectable at the edge of the observable Universe. With such an extremely high luminosity, GRBs are widely considered as powerful probes of high-redshift galaxies once given the knowledge of their physical origin. A phenomenological bimodal distribution of the observed burst duration (T_{90}) with a rough separation around 2 s (Kouveliotou et al. 1993), implies that these events are from two physically distinct progenitors. That is, long GRBs (LGRBs) with $T_{90} > 2$ s are expected to originate from the collapse of rapidly rotating massive stars (MacFadyen & Woosley 1999), and short GRBs (SGRBs) with $T_{90} < 2$ s are from mergers of compact stellar binaries (Narayan et al. 1992). Moreover, the detection of associations of many LGRBs with core-collapse supernovae (Hjorth et al. 2003; Woosley & Bloom 2006) as well as the preference of LGRBs to be located in star-forming galaxies (e.g. Le Floch et al. 2003; Savaglio et al. 2009) provides strong observational support to the collapsar model of LGRBs.

Due to the link between LGRBs and the death of massive stars, the redshift distribution of LGRBs can be used to study the cosmic star formation rate (CSFR). Especially at very high redshifts where only the most luminous galaxies are above the detection limit, LGRBs offer unique opportunities as tracers of star formation in faint galaxies, independent of galaxy luminosity and dust obscuration (see Salvaterra 2015; Schady 2017, for recent reviews). However, the way in which the LGRB rate traces the star formation is still very uncertain. The core-collapse single progenitor model for LGRBs predicts that low metallicity in the range of $Z < 0.1 - 0.3 Z_{\odot}$ is required for the retention of the angular momentum of the central core to launch the jet (Woosley & Heger 2006), while binary progenitor models typically imply a relatively modest metallicity dependence (Izzard et al. 2004; Fryer & Heger 2005; Podsiadlowski et al. 2010). A number of past studies (e.g. Kistler et al. 2008; Yüksel et al. 2008; Butler et al. 2010; Robertson & Ellis 2012) have compared the LGRB redshift distribution to the CSFR and concluded that the LGRB cosmic efficiency (i.e. the LGRB rate - CSFR ratio) increases rapidly with redshift over $z \lesssim 4$, which means that LGRBs are more frequent for a given CSFR at high redshifts.

Recent investigations of the observational data of host galaxies of LGRBs make the situation a controversial topic. Several studies have investigated the properties of LGRB hosts from unbiased and highly complete samples, such as the BAT6 (Salvaterra et al. 2012), TOUGH (Hjorth et al. 2012), and SHOALS (Perley et al. 2016a) samples. Based on these samples, studies focusing on the low redshifts ($z \lesssim 1.5$) suggest that LGRBs are in general produced preferentially in smaller, less massive and lower metallicity environments when compared to typical star-forming galaxies, although the very low metallicity thresholds expected from the single progenitor model are disfavored (e.g. Krühler et al. 2015; Vergani et al. 2015; Japelj et al. 2016; Perley et al. 2016b). It is also interesting to note that, at low redshifts, LGRBs are dominated by the so-called low-luminosity GRBs that may have different properties from the high redshift GRBs (e.g. Chapman et al. 2007; Liang et al. 2007), which produce a complex situation. The picture at higher redshifts is much less clear because of the smaller size of LGRB samples. Some studies (Greiner et al. 2015; Perley et al.

2016b) claimed that LGRBs can directly trace star formation at $z \gtrsim 3$, which can be explained by the fact that the average metallicity of star-forming galaxies drops steeply from $z = 0$ to $z \approx 3$. Meanwhile, Schulze et al. (2015) found that the LGRBs in a complete sample favor lower luminosity hosts at all comparable redshifts.

Alternatively, the properties of LGRB hosts have also been studied by various theoretical models, including numerical simulations and semi-analytical models. For example, Elliott et al. (2015) compared the results of high-resolution cosmological simulations with the observed LGRB sample, suggesting that the LGRB cosmic efficiency is about constant at $z > 5$. Meanwhile, Bignone et al. (2017) studied the properties of LGRB host galaxies by using a simulated LGRB host sample for $z < 3$, indicating that LGRB progenitors favor the existence of a metallicity threshold in the range of $0.3 - 0.6 Z_{\odot}$. Assuming that LGRBs could originate from both a collapsar and a metal independent channel, Trenti et al. (2015) found a moderate metallicity bias.

Although metallicity dependence has been expected to be the primary factor affecting the LGRB cosmic efficiency, it is not necessarily the only factor. Some other models have also been proposed to explain the nonconstant LGRB cosmic efficiency, including the redshift-dependent LGRB luminosity function (e.g. Virgili et al. 2011; Deng et al. 2016) and the redshift-dependent initial mass function of stars (e.g. Wang & Dai 2011). Moreover, there are several observational biases (e.g. Lien et al. 2014), the most important effect of which is from the flux limit of the satellite.

In our previous study (Hao & Yuan 2013), we compared the redshift distribution of Swift LGRBs from Robertson & Ellis (2012) with the predictions of several empirical star formation models, finding a moderate metallicity bias. Moreover, based on a self-consistent star formation model, we found that the difference between the CSFR and the LGRB rate could be explained as a consequence of LGRBs occurring in fainter galaxies. However, there are two main drawbacks in this work. First, the significance of the results is limited by the small number of LGRBs. Second, the adopted star formation model is too simple to be able to describe the chemical evolution in a self-consistent way.

In this paper, we gather redshifts and prompt emission properties for a large sample of Swift LGRBs detected before the end of 2017 and examine whether the intrinsic properties of these bursts in which we are interested are redshift-dependent. Then, by using the CSFR obtained from the state-of-the-art cosmological hydrodynamic simulation of galaxy formation, the Illustris simulation (Vogelsberger et al. 2014a,b), in which the star formation and metal enrichment are treated in a self-consistent way, we calculate the LGRB rate under different stellar metallicity thresholds. By comparing with our sample, we investigate the connection between the LGRB rate and star formation history to see if they can be used as an unbiased tracer of star formation history. In order to account for the effect of observational uncertainties, we also consider an empirical model of the CSFR based on observations. As a further test, we also compare the expected metallicity distribution of LGRB host galaxies with that of the observed host galaxies collected in the literature.

The paper is organized as follows. In Section 2, we describe our sample of LGRBs with known

redshifts and prompt emission properties that we are interested in. In Section 3, the possible redshift evolution of the LGRB luminosity distribution of our sample is checked. Section 4 outlines the methods used to calculate the LGRB rate. The results of the comparisons with observations are then shown in Section 5. Finally, conclusions and discussion are presented in Section 6.

2. LGRB sample

Over the last decade, the Swift has detected more than 1000 GRBs with peak fluxes in the 15 – 150 keV energy band and above the flux threshold of $\sim 1 \times 10^{-8} \text{ erg cm}^{-2} \text{ s}^{-1}$. About one third of these bursts have redshift measurements by the multiwavelength instruments on the satellite and follow-up observations through spectroscopy and photometry of the GRB afterglow or the host galaxy.

We select our sample among all the Swift LGRBs with known redshifts and prompt emission properties in the literature before the end of 2017. Note that some events found by the ground analysis but not by the satellite are removed, because their selections are done manually and lack systematicness. Ultra-long GRBs marked by Lien et al. (2016) are also excluded, since they may represent a distinct population of bursts that result from different progenitors, such as the tidal disruption events, magnetars, and low-metallicity blue supergiants (Gendre et al. 2013; Levan et al. 2014). We also exclude GRBs that are marked as SGRBs in Greiner’s online table ¹ where the classification also takes into account multiwavelength criteria, although their durations are longer than 2 s. The sample constructed this way consists of 371 Swift LGRBs, as listed in Table 1. We note that their durations (T_{90}), fluences within 15 – 150 keV (S), and peak photon fluxes (P) are taken from the online Swift/BAT GRB catalog ² (Lien et al. 2016).

One major selection effect for the observed redshift distribution of LGRBs is from the survey sensitivity of Swift’s detectors. However, the trigger criteria of Swift/BAT are very complicated, and there are two stages to this criteria. The “rate trigger” stage adopts over 500 “rate trigger” criteria, according to which a brighter burst has a higher trigger probability. In addition, an image will be generated for further confirmation and localization, the trigger of which also depends on the burst duration. A single explicit cut on prompt emission properties is commonly used for the purpose of measuring intrinsic redshift distributions. For example, Salvaterra et al. (2012) adopted a peak flux cut of $P \geq 2.6 \text{ ph s}^{-1} \text{ cm}^{-2}$, which corresponds to a peak flux that is ~ 6 times larger than the peak flux threshold of Swift/BAT. Nevertheless, the peak flux cut would affect the redshift distribution by removing more high redshift bursts with low-flux than that at low redshifts, while a fluence cut is suggested to have less influence on the redshift distribution (Perley et al. 2016a). Hence, we choose to adopt a fluence cut of $S_{15-150 \text{ keV}} \geq 1.0 \times 10^{-6} \text{ erg cm}^{-2}$, same as in Perley et al.

¹<http://www.mpe.mpg.de/~jcg/grbgen.html>

²<http://swift.gsfc.nasa.gov/results/batgrbcatalog/index.html>

(2016a). This further criterion selects 261 LGRBs, with a completeness in the redshift of 44 percent (261/597). Although the completeness of the sample with $P \geq 2.6 \text{ ph s}^{-1} \text{ cm}^{-2}$ in the redshift is 48 percent (112/235), which is slightly higher than the sample with the fluence cut, but the fluence cut criterion could provide a sample that has a much larger size. The cumulative redshift distribution of the fluence cut sample is shown in Figure 1. As can be seen, the redshift distribution of this sample is very similar to that of all known-redshift Swift LGRBs. In contrast, the redshift distribution of LGRBs with the peak flux cut shows an obvious excess of LGRBs at lower redshifts. The Anderson-Darling (A-D) k-sample test for consistency gives a $p = 0.02$ between this distribution with the peak flux cut and that with the fluence cut. For comparison, we also show the distribution of the complete SHOALS (Perley et al. 2016a) sample in Figure 1. It is worth stressing that although the completeness of our sample is not as high as the SHOALS sample, they show similar consistency.

From the redshift z and the fluence S , integrated over the observed Swift band (15-150 keV), we calculate the intrinsic isotropic energy E_{iso} , following the standard relation:

$$E_{\text{iso},45-450 \text{ keV}} = \frac{4\pi d_L^2 S_{15-150 \text{ keV}} k(z)}{1+z}, \quad (1)$$

where d_L is the luminosity distance and $k(z)$ is the k -correction for the fluence transferred from the observed detector band to its rest-frame. Following Perley et al. (2016a), in order to reduce the uncertainty due to Swift’s narrow bandpass, we only calculate the rest-frame energy range of 45-450 keV, which would make the k -correction much smaller and more reliable. In particular, its value is $k(z) = [(1+z)/(1+2)]^{-0.5}$. Figure 2 shows the isotropic energy-redshift distribution of our sample, in which the solid line indicates the energy threshold with $S_{\text{lim},15-150 \text{ keV}} = 1.0 \times 10^{-6} \text{ erg cm}^{-2}$. Then, the isotropic luminosity L_{iso} is estimated as

$$L_{\text{iso}} = \frac{E_{\text{iso},45-450 \text{ keV}}}{T_{90}/(1+z)}. \quad (2)$$

In Figure 3, the isotropic luminosity distribution is shown for bursts with the fluence cut. The solid line indicates the detection threshold of Swift, which has a flux limit of $\sim F_{\text{lim}} = 1.0 \times 10^{-8} \text{ erg cm}^{-2} \text{ s}^{-1}$.

3. Check for the luminosity evolution

In addition to the metallicity threshold, the cosmic evolution of the LGRB luminosity could be one of the explanations for the nonconstant LGRB cosmic efficiency. Here, with our relatively large sample, we first check whether such a cosmic evolution of the LGRB luminosity exists using a simple method. We divide our LGRB sample into seven redshift bins as $0 < z < 1$, $0.5 < z < 1.5$, $1 < z < 2$, $1.5 < z < 2.5$, $2 < z < 3$, $2.5 < z < 3.5$, and $3.0 < z < 4.0$. The adjacent bins are adopted to overlap with each other just to obtain a sufficiently large LGRB number for each redshift bin. In Figure 4, as a visualization of the redshift evolution, the cumulative luminosity distributions of LGRBs with $L_{\text{iso}} > 10^{51} \text{ erg s}^{-1}$ in various redshift bins are displayed. As can be

seen, the two lowest-redshift bins show an obvious lack of medium- to high-luminosity LGRBs, which may be due to their low event rate and the small observable volume at low redshifts. On the other hand, the remaining five curves between $1 < z < 4$ display similar consistency. The A-D test gives a $p = 0.83$ that these five distributions are drawn from the same parent distribution, which implies that there is little redshift evolution of the LGRB luminosity, at least between $1 < z < 4$. We also plot the cumulative distributions of isotropic energy in different redshift bins in Figure 5. These distributions show similar characteristics to that of the LGRB luminosity. Therefore, it is enough to assume a non-evolving luminosity function of LGRBs with $L_{\text{iso}} \gtrsim 10^{51} \text{ erg s}^{-1}$ for our purpose in this paper. We leave a more thorough investigation on the redshift evolution of the luminosity distribution to a future work.

4. LGRB formation rate

In this section, we estimate the rate of LGRB formation as a function of redshift. LGRBs are believed to result from the collapse of massive stars, making them good tracers of the star formation rate after taking into account the conditions necessary to affect the LGRB cosmic efficiency. Our estimations thus begin with the CSFR. In this paper, the CSFR is obtained from the Illustris simulation (Vogelsberger et al. 2014a; Genel et al. 2014), which is a large-scale cosmological hydrodynamical simulation of galaxy formation in a volume of $(106.5 \text{ Mpc})^3$ with a dark mass resolution of $6.26 \times 10^6 M_{\odot}$ and a baryonic mass resolution of $1.26 \times 10^6 M_{\odot}$. The dynamics of dark matter and gas are computed using the moving-mesh code AREPO (Springel 2010). The simulation adopted the following cosmological parameters: $\Omega_m = 0.2726$, $\Omega_{\Lambda} = 0.7274$, $\Omega_b = 0.0456$, $\sigma_8 = 0.809$, $n_s = 0.963$ and $h = 0.704$, consistent with the Wilkinson Microwave Anisotropy Probe (WMAP)-9 results (Hinshaw et al. 2013). In addition, the subgrid physical processes for galaxy formation employed by Illustris include gas cooling (primordial and metal-line cooling), stellar evolution and feedback processes, gas recycling, metal enrichment based on nine elements, and supermassive black hole growth and related active galactic nucleus (AGN) feedback processes in various modes. For full details of the models and the parameter selection see Vogelsberger et al. (2013) and Torrey et al. (2014). The simulation starts at redshift $z = 127$ and evolves to the present day ($z = 0$). Many of the key observables of the local Universe, such as the galaxy stellar mass and luminosity functions, baryon conversion efficiency and the morphology of galaxies, are reasonably well reproduced by the simulation, although not every observed property is matched precisely. There are still some discrepancies, such as the quenching of massive galaxies and the age distribution of low-mass galaxies (Vogelsberger et al. 2014a). The subgrid models of the simulation still need further improvements. Nevertheless, the simulation could provide us with useful insights on the physics of the Universe especially at high redshifts where direct observations are generally lacking.

The predicted global CSFR from the Illustris simulation is also in good agreement with the observations (Behroozi et al. 2013; Novak et al. 2017) up to $z \sim 8$, as shown in Figure 6. The slight excess of the simulated star formation at lower redshifts seems to be the result of insufficient AGN

feedback to quench star formation at these times, as indicated by Vogelsberger et al. (2014a). The contributions to the CSFR from stellar populations with metallicities below different thresholds ($Z_{\text{th}} = 0.3$ and $0.6 Z_{\odot}$, for example) are also shown, which can be easily used to deduce the preference of LGRBs for low-metallicity progenitors. As can be seen, a large fraction of new born stars have metallicities above the threshold of $Z_{\text{th}} = 0.6 Z_{\odot}$ at lower redshifts, while at $z \gtrsim 3$ most stars are born with metallicities below this value. In order to account for the uncertainty in the star formation history, we also plot the CSFR fits from Behroozi et al. (2013) and Madau & Dickinson (2014), respectively, in Figure 6.

If we assume that the progenitors of LGRBs are stars massive enough to form a black hole, the LGRB rate should follow the CSFR in a unbiased way. Then, the intrinsic cosmic LGRB rate can be related to the CSFR as

$$\dot{n}_{\text{LGRB}}(z) \propto \dot{\rho}_{\text{SFR}}(z). \quad (3)$$

Note that the time delayed between the formation of LGRBs and the progenitor stars is negligible, since massive stars are short-lived objects.

Adopting the CSFR from the Illustris simulation, a low-metallicity preference for LGRB progenitors could be simply described by considering only the new born stars with the metallicity below a given threshold (Z_{th}). Then, the intrinsic cosmic LGRB rate for a selected Z_{th} is

$$\dot{n}_{\text{LGRB}}(z) \propto \dot{\rho}_{\text{SFR}}(z, Z_{\text{th}}). \quad (4)$$

As a reference for the observational uncertainty, we also derive the intrinsic LGRB rate from the CSFR fit of Behroozi et al. (2013) as

$$\dot{n}_{\text{LGRB}}(z) \propto \Psi(z, Z_{\text{th}}) \dot{\rho}_{\text{SFR}}(z), \quad (5)$$

where $\Psi(z, Z_{\text{th}})$ is the fraction of star formation occurring in galaxies with a metallicity below Z_{th} , which is described by the following expression (Robertson & Ellis 2012):

$$\Psi(z, Z_{\text{th}}) = \frac{\int_0^{M_{\star, \text{crit}}(z, Z_{\text{th}})} \text{SFR}(M_{\star}, z) \phi(M_{\star}, z) dM_{\star}}{\int_0^{\infty} \text{SFR}(M_{\star}, z) \phi(M_{\star}, z) dM_{\star}}, \quad (6)$$

where $\text{SFR}(M_{\star}, z)$ is the SFR-stellar mass relation, $\phi(M_{\star}, z)$ is the galaxy stellar mass function, and $M_{\star, \text{crit}}(z, Z_{\text{th}})$ is the critical galaxy mass related to a metallicity threshold Z_{th} , which can be expressed by the so-called redshift-dependent mass-metallicity (M - Z) relation (Savaglio et al. 2005, on the scale of Kobulnicky & Kewley 2004)³

$$\begin{aligned} 12 + \log[\text{O}/\text{H}] &= -7.5903 + 2.5315 \log M_{\star} \\ &\quad - 0.09649 \log^2 M_{\star} \\ &\quad + 5.1733 \log t_{\text{u}} - 0.3944 \log^2 t_{\text{u}} \\ &\quad - 0.403 \log t_{\text{u}} \log M_{\star}, \end{aligned} \quad (7)$$

³The oxygen abundance $12 + \log[\text{O}/\text{H}]$ is related to the metallicity Z/Z_{\odot} by the scaling $12 + \log[\text{O}/\text{H}] = \log(Z/Z_{\odot}) + 8.69$ (Allende Prieto et al. 2001) throughout this paper.

where t_u is the age of the Universe at redshift z in Gyr and M_\star is the galaxy stellar mass in M_\odot . Tomczak et al. (2016) parameterized the redshift-dependent SFR-stellar mass relation at $0.5 < z < 4$ using data from the FourStar Galaxy Evolution Survey, based on the formula of Lee et al. (2015):

$$\log(\text{SFR}(M_\star, z)) = s_0 - \log \left[1 + \left(\frac{M_\star}{M_0} \right)^{-\gamma} \right], \quad (8)$$

where the best-fit parameters s_0 in $\log(M_\odot/\text{yr})$ and M_0 in M_\odot for star-forming galaxies are

$$\begin{aligned} s_0 &= 0.448 + 1.220z - 0.174z^2 \\ \log(M_0) &= 9.458 + 0.865z - 0.132z^2 \\ \gamma &= 1.091. \end{aligned}$$

For the redshift-evolving stellar mass function, we adopt the parameterization derived by Drory & Alvarez (2008):

$$\phi(M_\star, z) dM_\star = \phi_\star \left(\frac{M_\star}{M_1} \right)^\gamma \exp \left(-\frac{M_\star}{M_1} \right) \frac{dM_\star}{M_1}, \quad (9)$$

where the parametric functions obey

$$\begin{aligned} \phi_\star(z) &\approx 0.003(1+z)^{-1.07} \text{ Mpc}^{-3} \text{ dex}^{-1} \\ \log[M_1/M_\odot](z) &\approx 11.35 - 0.22 \ln(1+z) \\ \gamma &\approx -1.3. \end{aligned}$$

In Figure 7, we show the results of Equation (6) with different metallicity thresholds: $Z_{\text{th}} = 0.3, 0.6$ and $0.9 Z_\odot$. The results from the Illustris simulation are also plotted as a comparison. As can be seen, the empirical model shows that more than 80% of stars are formed in galaxies above $0.9 Z_\odot$ around $z = 0$, while the simulation predicts a somehow lower fraction ($\sim 60\%$) at the same redshift. The discrepancy between the simulation and the empirical model could come from various uncertainties. For instance, the empirical models are heavily dependent on the adopted functional form and observational data. Different empirical models can suggest very different imprints, as seen in our previous work (Hao & Yuan 2013). Also note that the empirical relations, such as the M - Z relation of Savaglio et al. (2005) are mainly based on the low redshift data, the validity of which at high redshifts needs to be tested and improved with future measurements. On the other hand, Bignone et al. (2017) indicated that the M - Z relation of the Illustris simulation presents, more or less, some differences with observations, although it could globally reproduce a large number of key LGRB host properties. However, a thorough investigation about this discrepancy is beyond the reach of this paper.

The expected redshift distribution of LGRBs is given by

$$\frac{dN}{dz} = A \dot{n}_{\text{LGRB}}(z, Z_{\text{th}}) \frac{dV/dz}{1+z}, \quad (10)$$

where the constant A depends on the observing time, the sky coverage, and so on. The comoving volume element dV/dz is calculated by

$$\frac{dV}{dz} = \frac{4\pi cd_L^2}{1+z} \left| \frac{dt}{dz} \right|, \quad (11)$$

where d_L is the luminosity distance and dt/dz is given by (Pereira & Miranda 2010)

$$\frac{dt}{dz} = \frac{9.78h^{-1}\text{Gyr}}{(1+z)\sqrt{\Omega_\Lambda + \Omega_m(1+z)^3}}. \quad (12)$$

Hence, the number of expected LGRBs in the redshift between z_1 and z_2 is

$$N(z_1, z_2) = A \int_{z_1}^{z_2} \dot{n}_{\text{LGRB}}(z, Z_{\text{th}}) \frac{dV/dz}{1+z} dz. \quad (13)$$

To remove the constant A , the cumulative redshift distribution of LGRBs can be expressed as

$$N(z_1 | < z | z_{\text{max}}) = \frac{N(z_1, z)}{N(z_1, z_{\text{max}})}. \quad (14)$$

5. Comparison with observations

5.1. Cumulative redshift distribution of LGRBs

Considering that the low-metallicity galaxies increasingly dominate the contribution to the CSFR at higher redshifts, even if a metallicity bias is present in the LGRB progenitors, the expected correction from the LGRB rate to the CSFR at high redshifts would be limited. In fact, the investigation of LGRB host galaxies over $3 < z < 5$ suggests that LGRBs are an unbiased star formation tracer from $z \approx 3$ out to the highest redshift (Greiner et al. 2015). Thus, we divide our LGRB sample into two components: a low-redshift sample in the range of $0 < z < 3$, and a high-redshift sample in the range $3 < z < 5$. In order to remove low-luminosity bursts that could not be detected at high redshifts, which is due to the selection effects from the Swift threshold, we choose a luminosity cut of $L_{\text{iso}} > 0.7 \times 10^{51} \text{ erg s}^{-1}$ for the low-redshift sample, which has 120 LGRBs left, while the luminosity cut is set to $L_{\text{iso}} > 2 \times 10^{51} \text{ erg s}^{-1}$ for the high-redshift sample, which includes 35 LGRBs.

The cumulative redshift distribution of the low-redshift sample between $0 < z < 3$ is shown in Figure 8. The solid red line is the expected LGRB distribution based on the Illustris CSFR with no metallicity threshold. The LGRB distributions inferred by adopting $Z_{\text{th}} = 0.3, 0.6,$ and $0.9 Z_\odot$, respectively, are shown in Figure 8 for instance. Whether a model distribution is consistent with that of the observed sample can be evaluated by the one-sample Kolmogorov-Smirnov (K-S) test. After considering the given metallicity thresholds: $Z_{\text{th}} = 0.1, 0.2, 0.3, \dots, 1.0 Z_\odot$, as well as the null hypothesis that there is no metallicity preference, we find that all metallicity thresholds

between $Z_{\text{th}} = 0.3 - 1.0 Z_{\odot}$ could produce K-S test $p > 0.1$. The maximum probability occurs at $Z_{\text{th}} = 0.9 Z_{\odot}$ (K-S test $p = 0.99$). Cases with no metallicity threshold or with an extreme threshold of $Z_{\text{th}} \leq 0.2 Z_{\odot}$ are disfavored (K-S test $p < 0.07$). This confirms the presence of a host galaxy metallicity threshold close to the solar value, above which LGRBs are suppressed (Robertson & Ellis 2012; Wang & Dai 2014; Perley et al. 2016b). On the other hand, for the high-redshift sample between $3 < z < 5$, we find that all metallicity thresholds produce K-S test $p > 0.49$ (Figure 9). This is somewhat not surprising, since at $z > 3$, most of the star formation occurs in galaxies of $Z \lesssim 0.6 Z_{\odot}$ (see Figure 6). This may imply that LGRBs could be used as unbiased tracers of star formation at high redshifts, in accordance with the analysis of host galaxies over $3 < z < 5$ by Greiner et al. (2015). Nevertheless, we caution that this conclusion is only tentative due to the small number of LGRBs in this redshift interval. The results of the K-S tests are summarized in Figure 10.

For comparison, we also calculate the expected cumulative redshift distribution of LGRBs using the empirical CSFR from Behroozi et al. (2013) together with Equation (6), for different metallicity threshold values. The results are shown in Figures 11 and 12, for low and high redshifts, respectively (see also Figure 10 for the K-S test results). Similar to the results from the Illustris simulation, we find that the region where K-S test $p > 0.1$ contains metallicity thresholds of $0.3 Z_{\odot} \leq Z_{\text{th}} \leq 1.0 Z_{\odot}$ and the maximum p -value occurs at $Z_{\text{th}} = 0.7 Z_{\odot}$ at $0 < z < 3$. For the redshift range between 3 and 5, all cases are consistent with the data (K-S test $p > 0.38$), which is also in accordance with the results from the Illustris simulation. It is interesting to note that, while the cumulative LGRB distribution for the metallicity threshold of $Z_{\text{th}} = 1.0 Z_{\odot}$ shows a good agreement with the observations, the result from a lower threshold of $Z_{\text{th}} = 0.3 Z_{\odot}$ presents similar consistency as well. However, the absolute metallicity distributions of LGRB progenitors would be quite different between these two thresholds. Therefore, a further test is necessary to understand their intrinsic metallicity preference, which will be executed in the next section.

5.2. Metallicity distribution of LGRB host galaxies

To further understand the effects of metallicity on the comparison of cumulative redshift distributions, here we investigate the metallicity distribution of LGRB host galaxies. Using Equation (13), we can simply estimate the number of stars being produced as a function of stellar metallicity. This result can then be compared with the metallicity distribution of LGRB host galaxies from the observations. For comparison, we collect a sample of LGRB host galaxies with metallicities determined by direct observations in the literature, including Krühler et al. (2015), Japelj et al. (2016), and GRB Host Studies (GHostS)⁴. As there are plenty unknown issues relating to the cosmic evolution, we would restrict our host sample to the $0 < z < 1$ range. The total number of LGRB host galaxies with measured metallicity is 42 and they are listed in Table 2. As shown in

⁴<http://www.grbhosts.org>

Figure 13, only nine LGRB host galaxies (21%) have super-solar metallicities, while most are well below the solar value.

In Figure 14, we compare the LGRB host metallicity distribution of our sample from $0 < z < 1$ with the predictions considering the contribution of the global CSFR, regardless of any bias, in the same redshift range. The expectations are normalized to the number of the observed hosts. Note that for the sake of simplicity, all hosts with super-solar metallicities ($Z > Z_{\odot}$) are plotted within the metallicity bin of $1 < Z/Z_{\odot} < 1.2$. As can be seen, for the Illustris simulation, the fraction of star formation above the solar metallicity is around 50%. The empirical model shows a similar result as well. Therefore, if LGRBs trace the star formation unbiasedly all the time, a significant fraction of their hosts should have super-solar metallicities, which is clearly inconsistent with the observations. These results confirm previous studies that, at least at lower redshifts, LGRB hosts prefer to occur in environments below the solar metallicity (e.g. Graham & Fruchter 2013; Vergani et al. 2015; Schulze et al. 2015; Perley et al. 2016b; Bignone et al. 2017). After considering a sharp metallicity threshold of $Z_{\text{th}} = Z_{\odot}$, we recalculated the CSFRs as a function of stellar metallicity, as shown in Figure 14. The peaks of the predicted distribution shift from $> Z_{\odot}$ to $\sim 0.8 Z_{\odot}$, which is much more consistent with the observational data. These results are roughly consistent with that found in the previous section by comparing the cumulative redshift distributions of LGRBs. Here for simplicity in these models, we adopted a sharp cutoff to represent the low-metallicity preference of LGRBs, but we note that LGRBs do occur in high-metallicity environments, which could be the results of the internal metallicity dispersion in galaxies (Niino 2011; Bignone et al. 2017), or may imply the existence of two channels of LGRB progenitors (Trenti et al. 2015).

6. Conclusions and discussion

In this paper, we have revisited the relationship between the LGRB rate and CSFR. For this purpose, we collected a large sample of 371 Swift LGRBs with known redshifts and prompt emission properties, which include the T_{90} duration, fluence and peak photon flux. A fluence cut of $S_{15-150 \text{ keV}} \geq 10^{-6} \text{ erg cm}^{-2}$ is used to reduce the selection effect of the sensitivity of the detectors. We pay special attention to the redshift evolution of the intrinsic emission properties of LGRBs, such as the isotropic luminosity and the isotropic energy. Based on our relatively large sample, we could investigate the cumulative luminosity distributions of LGRBs with $L_{\text{iso}} \gtrsim 10^{51} \text{ erg s}^{-1}$ in various redshift bins, finding that the distributions of these high-luminosity bursts show little evolution with redshift over $1 < z < 4$. Therefore, for reproducing the LGRB rate history in this paper, we choose to ignore the redshift evolution of LGRB luminosity function. Although given the influences of many unknown observational biases such as the GRB jet opening angle (e.g. Lu et al. 2012), a more thorough investigation on the redshift evolution of the luminosity distribution is still needed in the future.

Using the CSFR from the Illustris simulation, which is a large-scale cosmological hydrodynamical simulation, we have calculated the expected cumulative redshift distribution of LGRBs under

the assumption of the existence of host galaxies with different metallicity thresholds. The advantage of this kind of galaxy formation simulation is to allow us to consider the star formation and metallicity evolution of each individual galaxy in a self-consistent way. After comparing with our Swift sample, we find that all the predictions with the moderate threshold between $0.3 Z_{\odot} \leq Z_{\text{th}} \leq 1.0 Z_{\odot}$ can fit the data well at the redshift range between $0 < z < 3$. Models with no metallicity threshold or with an extreme threshold of $Z_{\text{th}} \leq 0.2 Z_{\odot}$ are disfavored. This is in rough agreement with previous studies arguing that at low redshifts, LGRBs have a tendency to occur in galaxies with a metallicity below the solar value (e.g. Modjaz et al. 2008; Robertson & Ellis 2012; Wang & Dai 2014; Vergani et al. 2015; Bignone et al. 2017). At higher redshifts over $3 < z < 5$, all metallicity thresholds can pass the K-S tests, implying that the observational data are consistent with no metallicity cutoff. Since most stars are born in environments of $Z \lesssim 0.6 Z_{\odot}$ at $z > 3$, the low-metallicity preference would disappear above this redshift given a modest threshold of Z_{th} . This may suggest that LGRBs trace all star formation directly at $z > 3$. The predictions from the empirical model also show similar results. Nevertheless, we caution that it may not be sufficient to claim a strict constraint on the metallicity threshold only through the comparison of cumulative LGRB redshift distributions, since models with a large range in metallicity thresholds exhibit similar consistency with the data.

To further test the low-metallicity preference of LGRBs, we have also calculated the metallicity distributions of star forming galaxies from different models and compared them with the observed LGRB host galaxies. Based on the results from the Illustris simulation and the empirical model, we confirm that at $z < 1$ a significant fraction of star forming galaxies are in super-solar environments ($\gtrsim 50\%$), which is clearly inconsistent with the metallicity distribution of the observed LGRB host galaxies. This result implies that the production of LGRBs in these high-metallicity galaxies is somehow suppressed. We also find that, by considering a metallicity threshold with $Z_{\text{th}} \lesssim Z_{\odot}$, this discrepancy could be partially alleviated.

Combining these results with the findings from the comparison of the redshift distribution of LGRBs, we conclude that at low redshifts LGRBs are more likely to occur in galaxies with metallicity below the solar value, consistent with the results of recent work (e.g. Perley et al. 2016b), which is higher than some of the previous theoretical works. While at $z \gtrsim 3$, given that a significant fraction of stars are born in sub-solar environments, LGRBs are good enough to be used as an unbiased tracer of the CSFR, at least to a first approximation.

Furthermore, more observations on LGRB host galaxies, especially at high redshifts, are desirable to constrain the theoretical models. Meanwhile, the detection of faint galaxies will also be needed to provide a detailed picture of the relationship between the LGRB and star formation. Given the difficulty of observing these objects at high redshifts from current detectors, next-generation observational facilities, such as the James Webb Space Telescope are anticipated to provide great insight into the nature of this relationship.

We thank the anonymous referee for her/his useful comments and suggestions that were helpful

for significantly improving the manuscript. This work is partially supported by the National Natural Science Foundation of China (grant Nos. 11503004, 11873056, 11390372, 11690024, 11991052, 11733001, 11725312, U1431228, 11421303, 11403006, and U1831119), and the Science and Technology Program of Guangzhou (201707010401).

REFERENCES

- Allende Prieto, C., Lambert, D. L., & Asplund, M. 2001, *ApJ*, 556, L63
- Behroozi, P. S., Wechsler, R. H., & Conroy, C. 2013, *ApJ*, 770, 57
- Bignone, L. A., Tissera, P. B., & Pellizza, L. J. 2017, *MNRAS*, 469, 4921
- Butler, N. R., Bloom, J. S., & Poznanski, D. 2010, *ApJ*, 711, 495
- Chapman, R., Tanvir, N. R., Priddey, R. S., & Levan, A. J. 2007, *MNRAS*, 382, L21
- Deng, C.-M., Wang, X.-G., Guo, B.-B., et al. 2016, *ApJ*, 820, 66
- Drory, N., & Alvarez, M. 2008, *ApJ*, 680, 41
- Elliott, J., Khochfar, S., Greiner, J., & Dalla Vecchia, C. 2015, *MNRAS*, 446, 4239
- Fryer, C. L., & Heger, A. 2005, *ApJ*, 623, 302
- Gendre, B., Stratta, G., Atteia, J. L., et al. 2013, *ApJ*, 766, 30
- Genel, S., Vogelsberger, M., Springel, V., et al. 2014, *MNRAS*, 445, 175
- Graham, J. F., & Fruchter, A. S. 2013, *ApJ*, 774, 119
- Greiner, J., Fox, D. B., Schady, P., et al. 2015, *ApJ*, 809, 76
- Hao, J.-M., & Yuan, Y.-F. 2013, *ApJ*, 772, 42
- Hinshaw, G., Larson, D., Komatsu, E., et al. 2013, *ApJS*, 208, 19
- Hjorth, J., Sollerman, J., Møller, P., et al. 2003, *Nature*, 423, 847
- Hjorth, J., Malesani, D., Jakobsson, P., et al. 2012, *ApJ*, 756, 187
- Izzard, R. G., Ramirez-Ruiz, E., & Tout, C. A. 2004, *MNRAS*, 348, 1215
- Japelj, J., Vergani, S. D., Salvaterra, R., et al. 2016, *A&A*, 590, A129
- Kistler, M. D., Yüksel, H., Beacom, J. F., & Stanek, K. Z. 2008, *ApJ*, 673, L119
- Kobulnicky, H. A., & Kewley, L. J. 2004, *ApJ*, 617, 240

- Kouveliotou, C., Meegan, C. A., Fishman, G. J., et al. 1993, *ApJ*, 413, L101
- Krühler, T., Malesani, D., Fynbo, J. P. U., et al. 2015, *A&A*, 581, A125
- Le Floc'h, E., Duc, P.-A., Mirabel, I. F., et al. 2003, *A&A*, 400, 499
- Lee, N., Sanders, D. B., Casey, C. M., et al. 2015, *ApJ*, 801, 80
- Levan, A. J., Tanvir, N. R., Starling, R. L. C., et al. 2014, *ApJ*, 781, 13
- Liang, E., Zhang, B., Virgili, F., & Dai, Z. G. 2007, *ApJ*, 662, 1111
- Lien, A., Sakamoto, T., Gehrels, N., et al. 2014, *ApJ*, 783, 24
- Lien, A., Sakamoto, T., Barthelmy, S. D., et al. 2016, *ApJ*, 829, 7
- Lu, R.-J., Wei, J.-J., Qin, S.-F., & Liang, E.-W. 2012, *ApJ*, 745, 168
- MacFadyen, A. I., & Woosley, S. E. 1999, *ApJ*, 524, 262
- Madau, P., & Dickinson, M. 2014, *ARA&A*, 52, 415
- Modjaz, M., Kewley, L., Kirshner, R. P., et al. 2008, *AJ*, 135, 1136
- Narayan, R., Paczynski, B., & Piran, T. 1992, *ApJ*, 395, L83
- Niino, Y. 2011, *MNRAS*, 417, 567
- Novak, M., Smolčić, V., Delhaize, J., et al. 2017, *A&A*, 602, A5
- Pereira, E. S., & Miranda, O. D. 2010, *MNRAS*, 401, 1924
- Perley, D. A., Krühler, T., Schulze, S., et al. 2016a, *ApJ*, 817, 7
- Perley, D. A., Tanvir, N. R., Hjorth, J., et al. 2016b, *ApJ*, 817, 8
- Podsiadlowski, P., Ivanova, N., Justham, S., & Rappaport, S. 2010, *MNRAS*, 406, 840
- Robertson, B. E., & Ellis, R. S. 2012, *ApJ*, 744, 95
- Salvaterra, R. 2015, *Journal of High Energy Astrophysics*, 7, 35
- Salvaterra, R., Campana, S., Vergani, S. D., et al. 2012, *ApJ*, 749, 68
- Savaglio, S., Glazebrook, K., & Le Borgne, D. 2009, *ApJ*, 691, 182
- Savaglio, S., Glazebrook, K., Le Borgne, D., et al. 2005, *ApJ*, 635, 260
- Schady, P. 2017, *Royal Society Open Science*, 4, 170304
- Schulze, S., Chapman, R., Hjorth, J., et al. 2015, *ApJ*, 808, 73

- Springel, V. 2010, MNRAS, 401, 791
- Tomczak, A. R., Quadri, R. F., Tran, K.-V. H., et al. 2016, ApJ, 817, 118
- Torrey, P., Vogelsberger, M., Genel, S., et al. 2014, MNRAS, 438, 1985
- Trenti, M., Perna, R., & Jimenez, R. 2015, ApJ, 802, 103
- Vergani, S. D., Salvaterra, R., Japelj, J., et al. 2015, A&A, 581, A102
- Virgili, F. J., Zhang, B., Nagamine, K., & Choi, J.-H. 2011, MNRAS, 417, 3025
- Vogelsberger, M., Genel, S., Sijacki, D., et al. 2013, MNRAS, 436, 3031
- Vogelsberger, M., Genel, S., Springel, V., et al. 2014a, MNRAS, 444, 1518
- . 2014b, Nature, 509, 177
- Wang, F. Y., & Dai, Z. G. 2011, ApJ, 727, L34
- . 2014, ApJS, 213, 15
- Woosley, S. E., & Bloom, J. S. 2006, ARA&A, 44, 507
- Woosley, S. E., & Heger, A. 2006, ApJ, 637, 914
- Yüksel, H., Kistler, M. D., Beacom, J. F., & Hopkins, A. M. 2008, ApJ, 683, L5

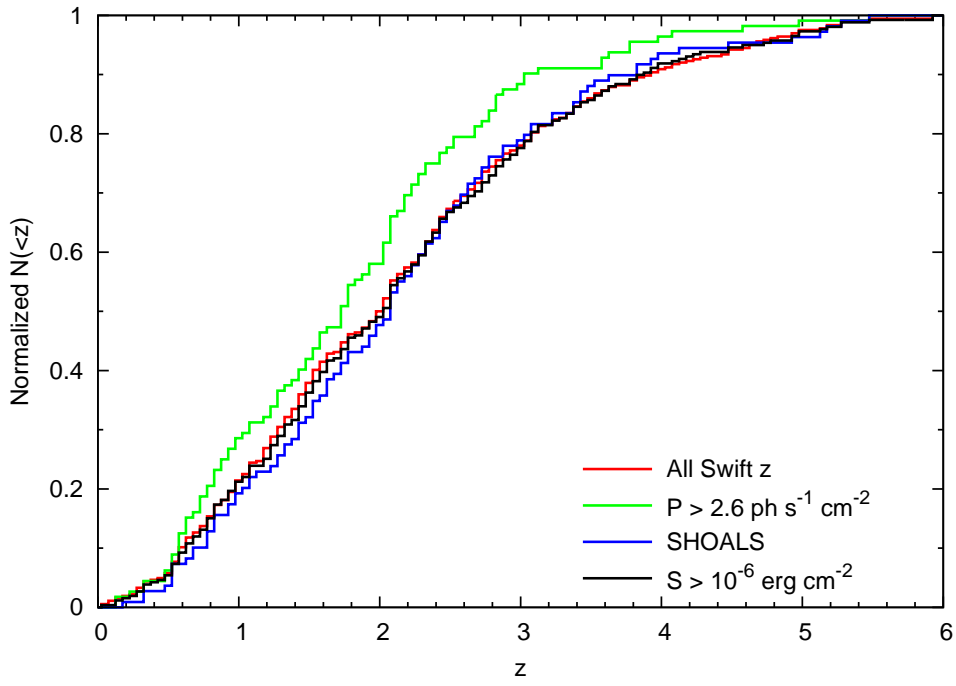


Fig. 1.— Cumulative redshift distribution of our sample with a fluence cut ($S_{15-150\text{keV}} > 10^{-6}\text{erg cm}^{-2}$) over $0 < z < 6$ compared to other LGRB samples, including the overall distribution of 371 Swift LGRBs with known redshifts, the SHOALS sample and so on.

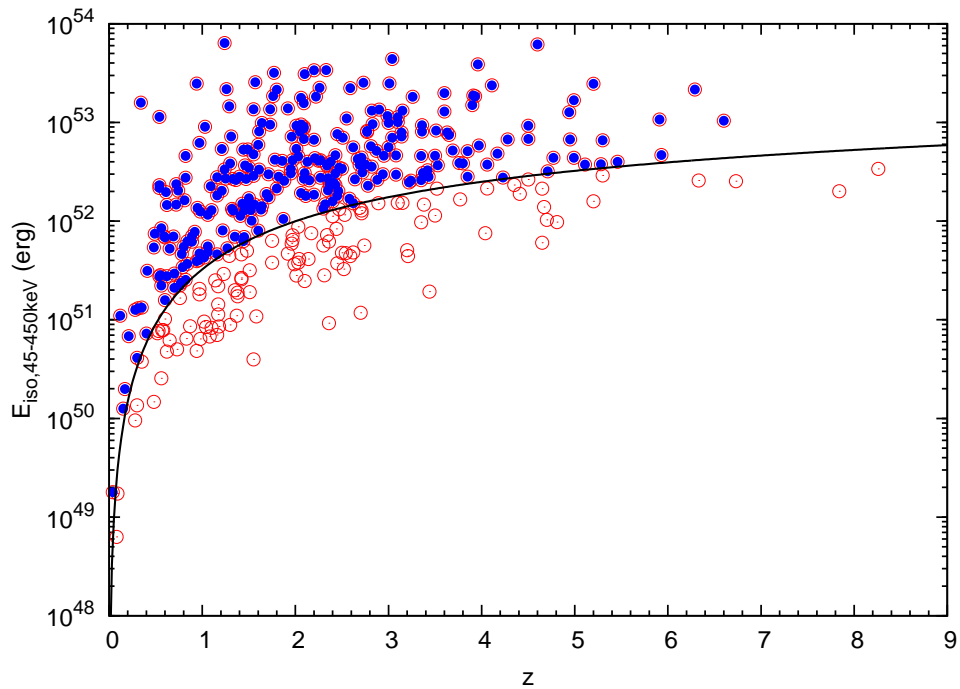


Fig. 2.— Isotropic energy vs. redshift distribution of 371 Swift LGRBs. The blue filled circles represent the LGRBs with a fluence cut, while the red empty circles represent all LGRBs with known redshifts. The solid line represents the energy threshold with $S_{\text{lim},15-150\text{keV}} = 10^{-6} \text{ erg cm}^{-2}$.

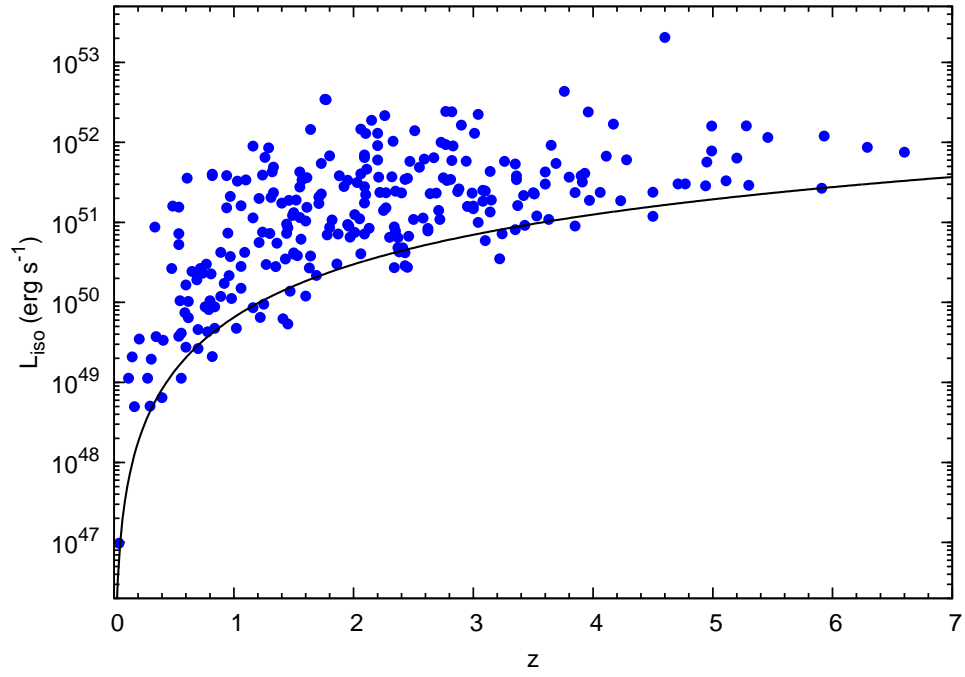


Fig. 3.— Isotropic luminosity vs. redshift distribution of LGRBs with the fluence cut. The solid line represents the detection threshold of Swift, which has a flux limit of $\sim F_{\text{lim}} = 1.0 \times 10^{-8} \text{ erg cm}^{-2} \text{ s}^{-1}$.

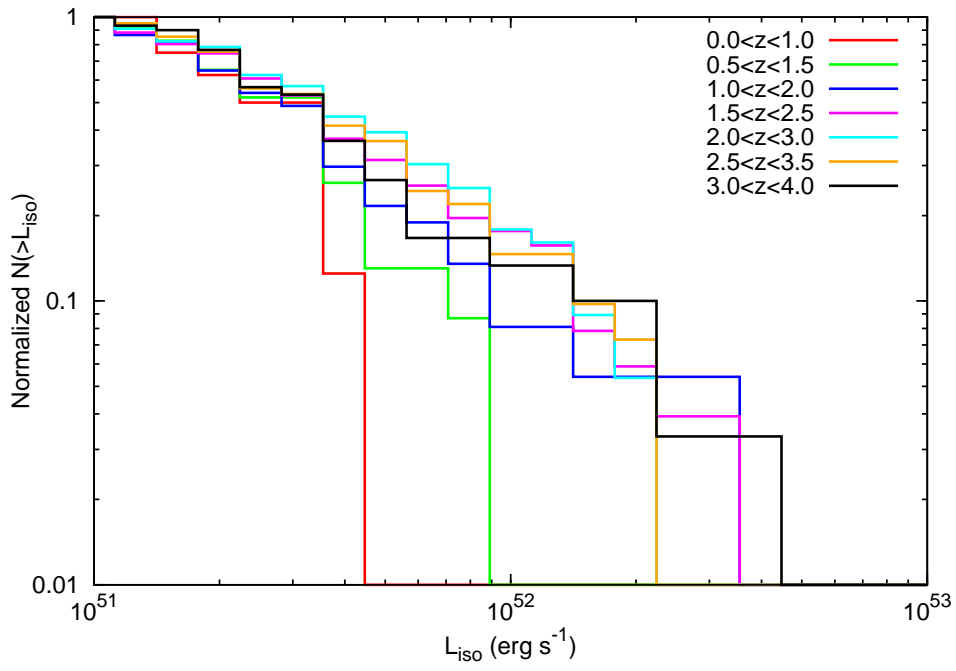


Fig. 4.— Cumulative luminosity distributions of LGRBs with $L_{\text{iso}} > 10^{51} \text{ erg s}^{-1}$ in seven different redshift bins.

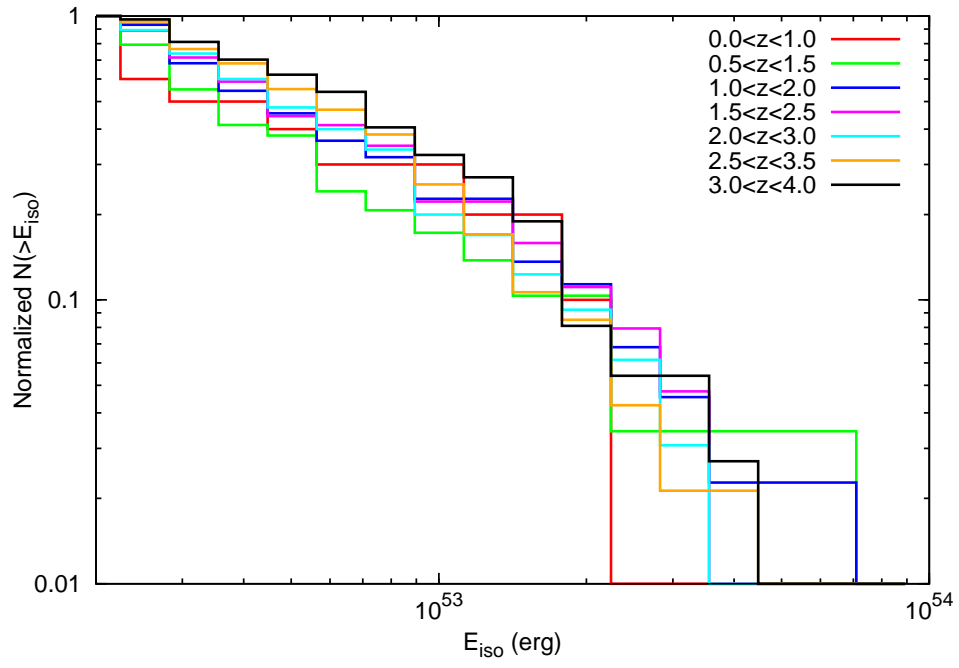


Fig. 5.— Same as Figure 4, but for the isotropic energy of LGRBs with $E_{\text{iso}} > 2 \times 10^{52}$ erg.

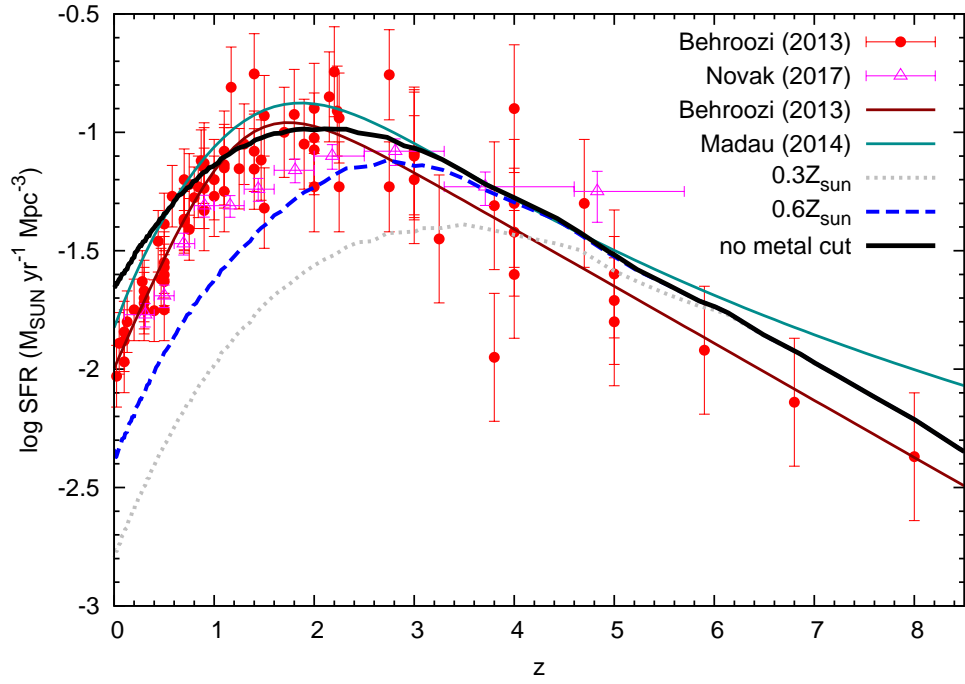


Fig. 6.— Cosmic star formation rate from the Illustris simulation and estimations with galaxy stellar metallicities below a certain value: 0.3 and 0.6 Z_{\odot} . The observational data are taken from UV+IR measurements (Behroozi et al. 2013) and radio measurements (Novak et al. 2017). As a reference, we also plot the empirical fit of Behroozi et al. (2013) and the CSFR of Madau & Dickinson (2014).

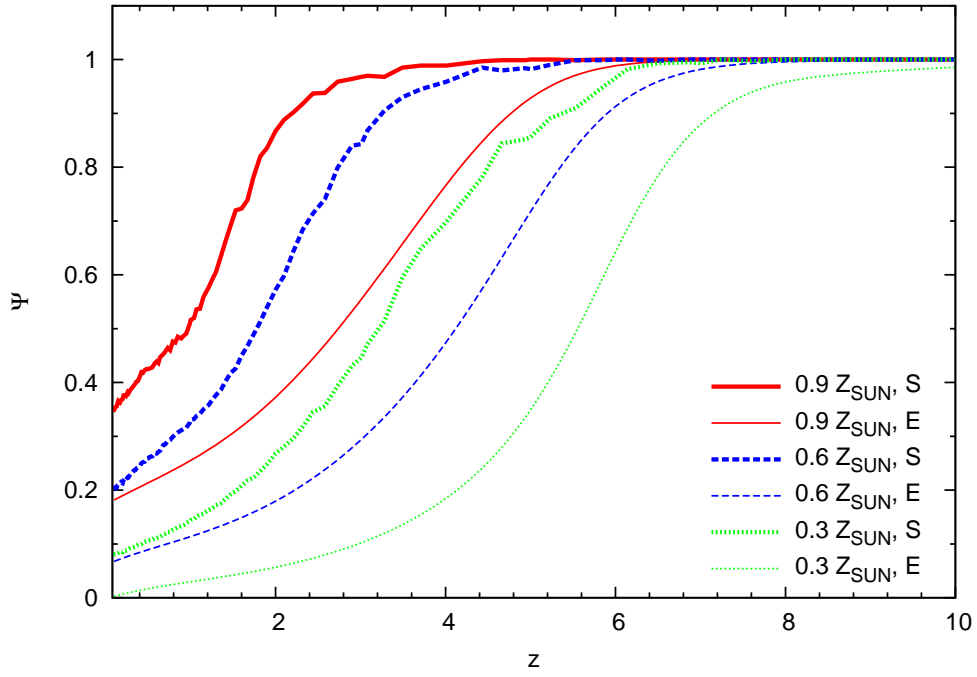


Fig. 7.— Fraction of star formation occurring in galaxies below a given metallicity threshold of Z/Z_{\odot} as a function of redshift (denoted as E). As a reference, we also plot the corresponding results from the Illustris simulation (denoted as S).

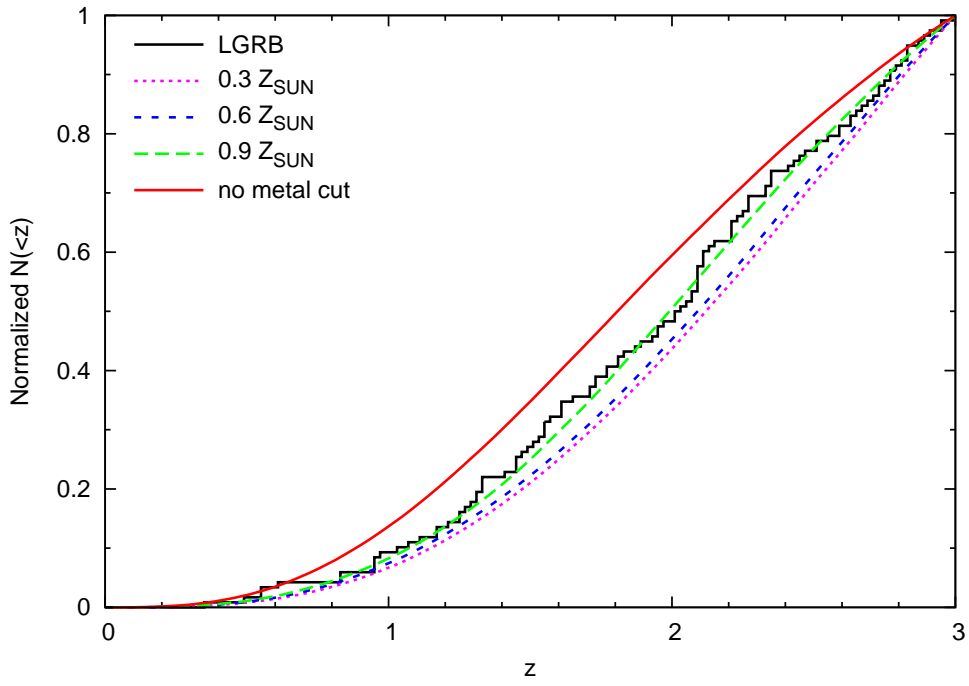


Fig. 8.— Cumulative redshift distribution of 120 Swift LGRBs with $L_{\text{iso}} > 0.7 \times 10^{51} \text{ erg s}^{-1}$ between $0 < z < 3$. The expected distributions are calculated using the CSFR from the Illustris simulation, for different metallicity thresholds.

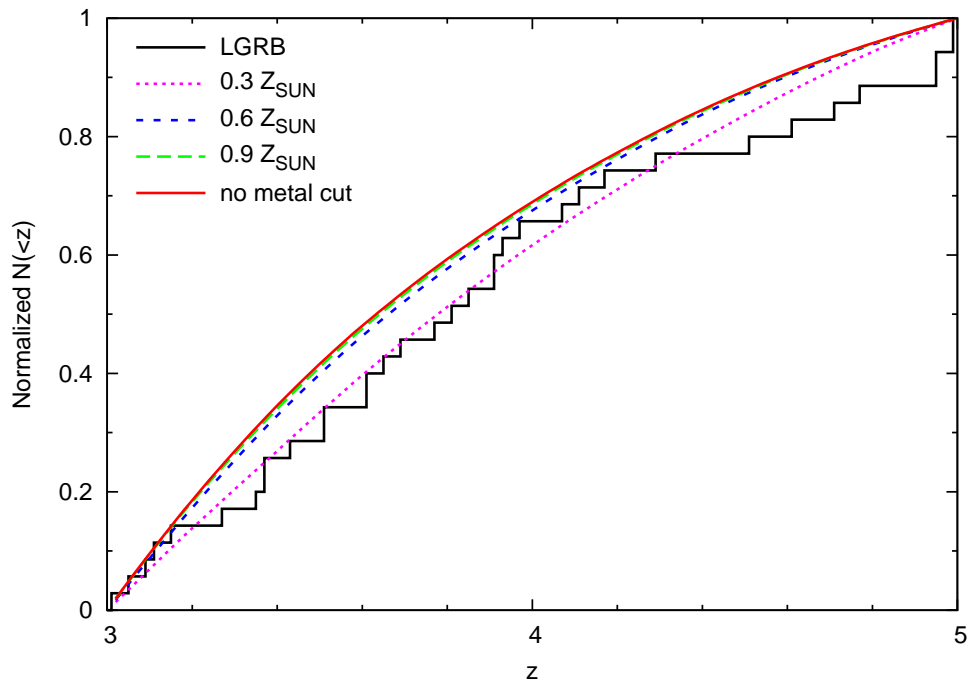


Fig. 9.— Cumulative redshift distribution of 35 Swift LGRBs with $L_{\text{iso}} > 2 \times 10^{51} \text{ erg s}^{-1}$ between $3 < z < 5$. The expected distributions are inferred from the Illustris simulation.

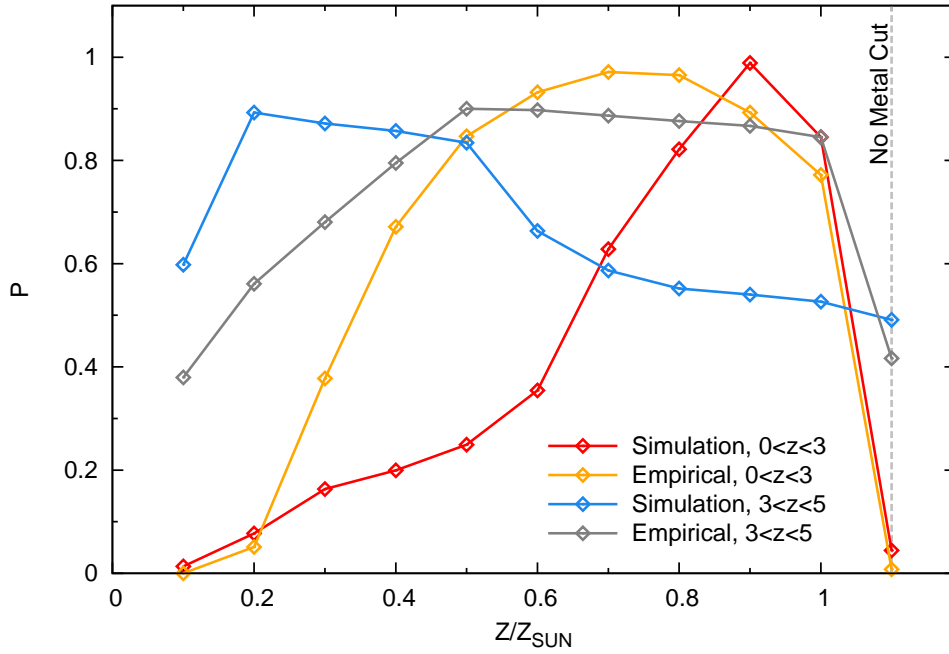


Fig. 10.— Results of the K-S tests comparing different expected cumulative redshift distributions with the observed LGRB samples. The p -values of consistency are calculated by assuming different metallicity thresholds for LGRB production: $Z_{\text{th}} = 0.1, 0.2, 0.3, \dots, 1.0 Z_{\odot}$, as well as the null hypothesis that no metallicity preference exists. Note that the rightmost points of these lines are for the cases with no metal cutoff.

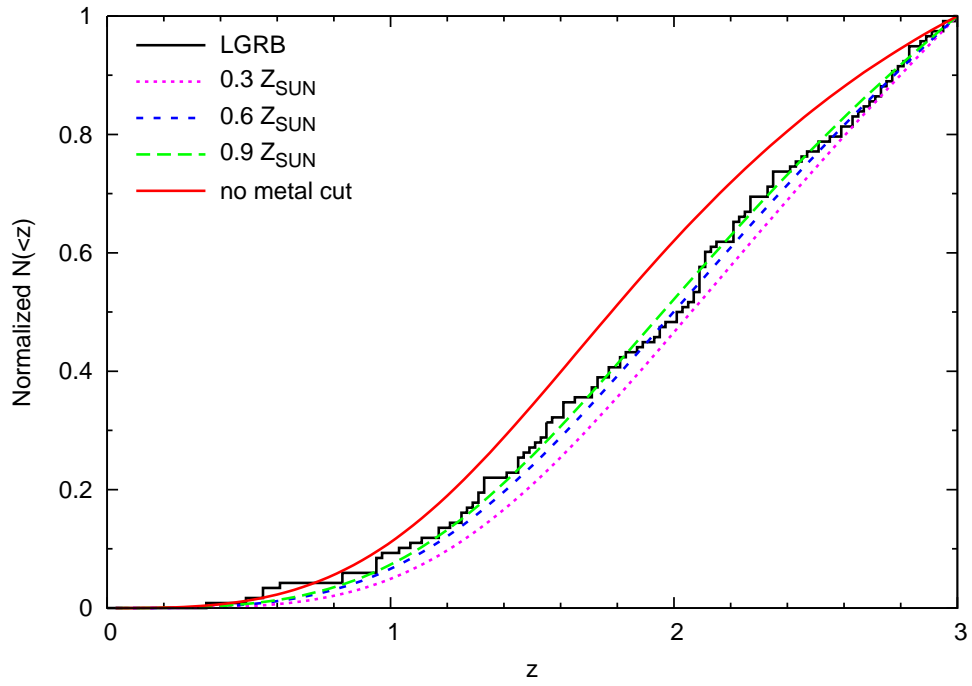


Fig. 11.— Same as Figure 8, but for the empirical model.

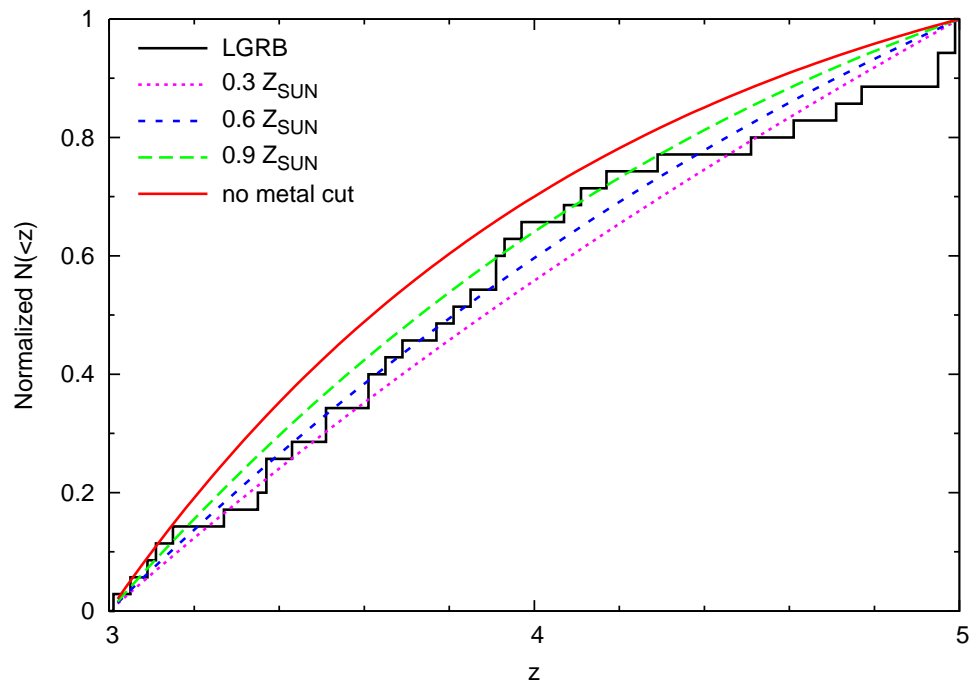


Fig. 12.— Same as Figure 9, but for the empirical model.

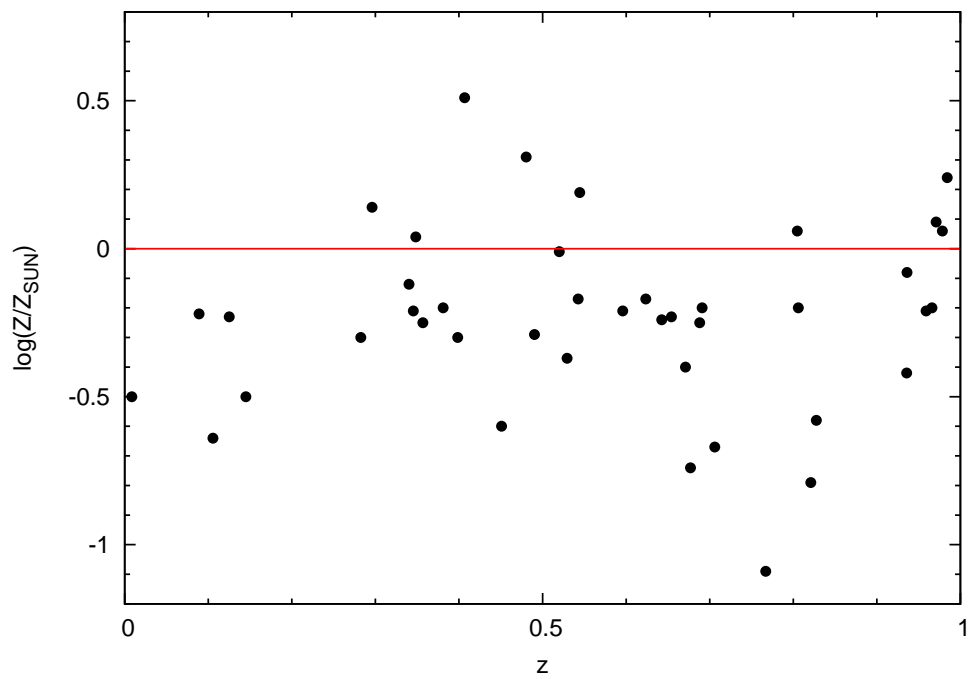


Fig. 13.— Metallicity vs. redshift distribution of 42 LGRB host galaxies between $0 < z < 1$. The red solid line represents the solar value Z_{\odot} .

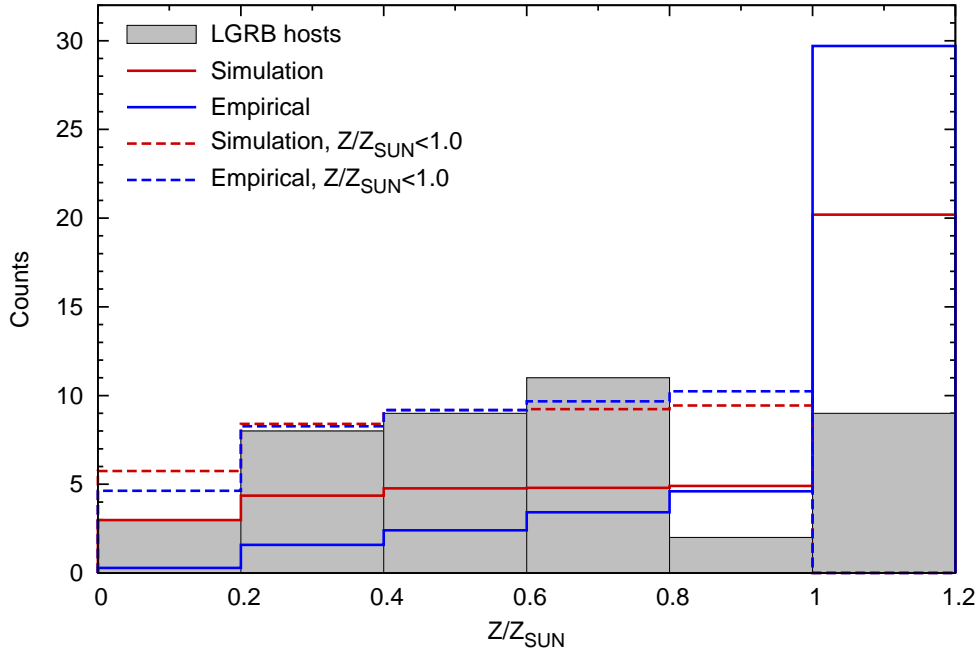


Fig. 14.— LGRB host galaxy metallicity distribution between $0 < z \leq 1$. The red and blue histograms are the expectations from the Illustris simulation and the empirical model, respectively, assuming LGRBs trace all star formation equally, while the red and blue dashed ones represent the distributions with a sharp metallicity cutoff of $Z_{\text{th}} = Z_{\odot}$.

Table 1. The List of 371 Swift LGRBs

GRB	z	T_{90} (s)	S (10^{-7} erg cm^{-2})	P ($\text{ph s}^{-1} \text{cm}^{-2}$)	$\log(E_{\text{iso}})$ (erg)	$\log(L_{\text{iso}})$ (erg s^{-1})	Refs.
GRB171222A	2.409	173.87	18.80	0.67	52.39	50.68	1
GRB171205A	0.037	190.47	35.30	0.95	49.25	46.99	1
GRB171020A	1.87	41.86	11.60	0.73	52.02	50.86	1
GRB170903A	0.886	27.72	23.60	3.91	51.79	50.62	1
GRB170705A	2.01	223.20	92.20	13.56	52.97	51.10	1
GRB170607A	0.557	320.00	76.30	2.71	51.93	49.62	1
GRB170604A	1.329	26.53	50.90	4.25	52.43	51.37	1
GRB170531B	2.366	170.30	19.20	0.75	52.39	50.68	1
GRB170519A	0.818	220.25	11.20	0.68	51.41	49.32	1
GRB170405A	3.51	165.31	38.80	...	52.92	51.35	1
GRB170202A	3.645	37.76	33.40	4.75	52.87	51.96	1
GRB170113A	1.968	20.30	6.63	1.07	51.81	50.97	1
GRB161219B	0.1475	6.93	15.40	5.30	50.10	49.32	1
GRB161129A	0.645	35.54	35.90	3.31	51.72	50.39	4
GRB161117A	1.549	125.70	202.00	6.81	53.13	51.44	1
GRB161108A	1.159	115.84	11.00	0.60	51.66	49.93	1
GRB161017A	2.013	217.05	53.70	2.81	52.73	50.88	1
GRB161014A	2.823	23.00	22.10	2.68	52.55	51.77	1
GRB160804A	0.736	152.74	109.00	2.84	52.31	50.37	1
GRB160425A	0.555	304.60	20.10	2.83	51.35	49.05	1
GRB160327A	4.99	33.74	13.60	1.70	52.64	51.89	1
GRB160314A	0.726	8.73	2.75	0.91	50.70	50.00	1
GRB160228A	1.64	98.91	19.30	1.17	52.15	50.58	3
GRB160227A	2.38	316.35	31.20	0.61	52.60	50.63	1
GRB160203A	3.52	17.44	9.93	1.29	52.33	51.74	1
GRB160131A	0.972	327.75	201.00	0.30	52.79	50.57	1
GRB160121A	1.96	10.50	6.13	1.18	51.77	51.22	1
GRB160117B	0.87	11.54	3.38	1.73	50.93	50.14	1
GRB151215A	2.59	17.85	3.08	1.59	51.65	50.95	1
GRB151031A	1.167	5.00	3.37	1.72	51.15	50.79	1
GRB151029A	1.423	8.95	4.37	1.73	51.41	50.84	1
GRB151027B	4.063	80.00	14.70	0.25	52.57	51.38	1
GRB151027A	0.81	129.58	72.90	6.85	52.21	50.36	1
GRB151021A	2.33	110.06	274.00	9.74	53.53	52.01	1
GRB150915A	1.968	160.00	7.38	0.18	51.86	50.12	1
GRB150910A	1.36	112.27	47.70	1.07	52.42	50.74	1
GRB150821A	0.755	168.94	8.44	...	51.22	49.24	1
GRB150818A	0.282	143.06	42.60	2.35	51.10	49.05	1
GRB150727A	0.313	87.96	36.10	1.04	51.12	49.29	1
GRB150413A	3.139	243.60	42.70	1.67	52.90	51.13	1
GRB150403A	2.06	37.30	171.00	0.98	53.25	52.16	1
GRB150323A	0.593	149.73	56.00	4.61	51.85	49.87	1
GRB150314A	1.758	14.78	225.00	37.99	53.27	52.54	1
GRB150301B	1.5169	17.14	19.80	3.01	52.11	51.28	1
GRB150206A	2.087	75.00	148.00	10.06	53.20	51.81	1

Table 1—Continued

GRB	z	T_{90} (s)	S (10^{-7} erg cm $^{-2}$)	P (ph s $^{-1}$ cm $^{-2}$)	$\log(E_{\text{iso}})$ (erg)	$\log(L_{\text{iso}})$ (erg s $^{-1}$)	Refs.
GRB150120B	3.5	24.34	5.34	1.22	52.06	51.32	3
GRB141225A	0.915	86.15	28.10	1.35	51.89	50.24	1
GRB141221A	1.452	36.82	21.10	3.06	52.11	50.93	1
GRB141220A	1.32	7.23	25.60	0.26	52.12	51.63	1
GRB141121A	1.47	481.00	43.20	0.88	52.43	50.14	1
GRB141109A	2.993	200.19	66.60	2.41	53.06	51.36	1
GRB141026A	3.35	139.48	12.90	0.36	52.41	50.91	1
GRB141004A	0.573	3.92	6.68	6.13	50.89	50.50	1
GRB140907A	1.21	80.00	45.10	1.57	52.31	50.75	1
GRB140710A	0.558	3.00	2.29	1.48	50.41	50.12	1
GRB140703A	3.14	68.64	38.80	2.77	52.86	51.64	1
GRB140629A	2.275	38.27	22.90	4.32	52.44	51.37	1
GRB140614A	4.233	77.39	10.30	0.32	52.44	51.27	1
GRB140518A	4.707	60.52	10.60	0.97	52.51	51.48	1
GRB140515A	6.33	23.42	6.19	0.91	52.41	51.91	1
GRB140512A	0.725	154.11	130.00	6.05	52.37	50.42	1
GRB140509A	2.4	23.22	12.30	1.55	52.20	51.37	1
GRB140506A	0.889	111.10	26.60	10.64	51.85	50.08	1
GRB140430A	1.6	173.59	11.30	2.50	51.90	50.08	1
GRB140428A	4.7	17.42	3.40	0.64	52.01	51.53	1
GRB140423A	3.26	134.14	93.70	2.15	53.26	51.76	1
GRB140419A	3.956	80.08	157.00	4.50	53.59	52.38	1
GRB140331A	4.65	209.66	7.13	0.22	52.33	50.76	1
GRB140318A	1.02	7.60	2.85	0.54	50.98	50.41	1
GRB140311A	4.954	70.48	21.00	1.28	52.83	51.75	1
GRB140304A	5.283	14.78	11.00	1.66	52.58	52.21	1
GRB140301A	1.416	27.80	4.55	0.81	51.42	50.36	1
GRB140213A	1.2076	59.93	120.00	23.55	52.73	51.30	1
GRB140206A	2.73	94.19	164.00	19.95	53.40	52.00	1
GRB140114A	3	139.95	32.00	0.95	52.75	51.20	1
GRB131227A	5.3	17.99	8.41	1.15	52.46	52.01	1
GRB131117A	4.042	10.88	2.98	0.66	51.88	51.54	1
GRB131103A	0.5955	15.21	8.12	1.56	51.01	50.03	1
GRB131030A	1.293	39.42	291.00	28.09	53.17	51.93	1
GRB130907A	1.238	364.37	1360.00	1.27	53.80	51.59	1
GRB130831A	0.4791	30.19	65.00	13.56	51.73	50.42	1
GRB130701A	1.155	4.38	43.80	17.10	52.26	51.95	1
GRB130612A	2.006	4.00	2.81	1.62	51.45	51.33	1
GRB130610A	2.092	47.72	25.30	1.72	52.43	51.24	1
GRB130606A	5.9134	276.66	27.60	2.51	53.03	51.43	1
GRB130604A	1.06	76.28	15.40	0.77	51.74	50.17	1
GRB130528A	1.25	640.00	56.80	0.25	52.43	49.98	1
GRB130514A	3.6	214.19	90.00	2.93	53.30	51.63	1
GRB130511A	1.3033	2.74	1.74	1.26	50.95	50.87	1
GRB130505A	2.27	89.34	34.70	...	52.62	51.18	1

Table 1—Continued

GRB	z	T_{90} (s)	S (10^{-7} erg cm^{-2})	P ($\text{ph s}^{-1} \text{cm}^{-2}$)	$\log(E_{\text{iso}})$ (erg)	$\log(L_{\text{iso}})$ (erg s^{-1})	Refs.
GRB130427B	2.78	25.90	14.50	3.15	52.36	51.52	1
GRB130427A	0.3399	244.33	3730.00	358.63	53.20	50.94	1
GRB130420A	1.297	121.14	75.90	3.33	52.58	50.86	1
GRB130418A	1.218	274.92	17.70	0.67	51.91	49.81	1
GRB130408A	3.758	4.24	16.70	5.12	52.59	52.64	1
GRB130215A	0.597	66.22	54.00	2.58	51.83	50.22	1
GRB130131B	2.539	4.30	3.38	0.96	51.67	51.59	1
GRB121229A	2.707	111.46	8.40	0.43	52.11	50.63	1
GRB121217A	3.1	778.09	61.70	1.75	53.05	50.77	1
GRB121211A	1.023	182.70	12.70	1.02	51.63	49.68	1
GRB121209A	2.1	42.92	28.70	3.38	52.49	51.35	1
GRB121201A	3.385	38.00	7.20	0.80	52.17	51.23	1
GRB121128A	2.2	23.43	58.30	12.46	52.82	51.96	1
GRB121024A	2.298	67.97	11.00	1.37	52.13	50.81	1
GRB120923A	7.84	26.08	3.89	0.63	52.30	51.83	1
GRB120922A	3.1	168.22	55.20	1.69	53.00	51.39	1
GRB120909A	3.93	220.60	75.00	1.81	53.26	51.61	1
GRB120907A	0.97	6.08	5.88	2.86	51.26	50.77	1
GRB120815A	2.3586	7.23	4.92	2.23	51.79	51.46	1
GRB120811C	2.671	24.34	28.40	3.96	52.63	51.81	1
GRB120805A	3.1	48.00	8.41	0.17	52.19	51.12	1
GRB120802A	3.796	50.29	16.40	3.03	52.59	51.57	1
GRB120729A	0.8	93.93	25.10	2.81	51.74	50.02	1
GRB120724A	1.48	77.92	8.00	0.72	51.70	50.20	1
GRB120722A	0.9586	36.32	13.30	1.00	51.60	50.34	1
GRB120714B	0.3984	157.31	12.50	0.35	50.86	48.81	1
GRB120712A	4.1745	14.81	18.40	2.30	52.69	52.23	1
GRB120624B	2.1974	179.66	296.00	5.39	53.53	51.78	1
GRB120521C	5.93	27.07	12.00	1.92	52.67	52.08	1
GRB120422A	0.28253	60.35	3.22	0.57	49.98	48.31	1
GRB120404A	2.876	38.72	15.80	1.16	52.42	51.42	1
GRB120401A	4.5	130.27	9.21	0.38	52.42	51.05	1
GRB120327A	2.8145	63.53	35.70	3.88	52.76	51.54	1
GRB120326A	1.798	69.48	25.20	4.74	52.33	50.94	1
GRB120224A	1.1	7.00	2.16	0.85	50.92	50.40	1
GRB120211A	2.4	64.32	8.62	0.46	52.05	50.77	1
GRB120119A	1.728	68.00	170.00	9.69	53.13	51.74	1
GRB120118B	2.943	20.30	17.50	2.16	52.48	51.76	1
GRB111229A	1.3805	25.37	3.36	0.97	51.28	50.25	1
GRB111228A	0.71627	101.24	82.70	12.23	52.17	50.40	1
GRB111225A	0.297	105.73	12.60	0.65	50.61	48.70	1
GRB111129A	1.0796	8.48	1.82	0.92	50.83	50.22	1
GRB111123A	3.1516	290.00	71.00	0.89	53.12	51.28	1
GRB111107A	2.893	31.07	9.12	1.24	52.18	51.28	1
GRB111008A	4.99005	62.85	52.00	6.42	53.22	52.20	1

Table 1—Continued

GRB	z	T_{90} (s)	S (10^{-7} erg cm $^{-2}$)	P (ph s $^{-1}$ cm $^{-2}$)	$\log(E_{\text{iso}})$ (erg)	$\log(L_{\text{iso}})$ (erg s $^{-1}$)	Refs.
GRB111005A	0.01326	23.21	5.75	1.13	47.56	46.20	1
GRB110818A	3.36	102.84	39.90	1.57	52.91	51.53	1
GRB110808A	1.348	40.70	3.69	0.58	51.30	50.06	1
GRB110801A	1.858	385.26	45.60	1.01	52.61	50.48	1
GRB110731A	2.83	40.94	59.40	10.67	52.98	51.95	1
GRB110726A	1.036	5.16	2.45	1.01	50.93	50.52	1
GRB110715A	0.8224	13.00	120.00	52.42	52.44	51.59	1
GRB110503A	1.613	58.70	113.00	29.63	52.91	51.56	1
GRB110422A	1.77	25.78	383.00	28.88	53.50	52.53	1
GRB110213A	1.4607	48.00	59.70	1.56	52.56	51.27	1
GRB110205A	2.22	249.42	158.00	3.12	53.26	51.37	1
GRB110128A	2.339	14.15	5.78	0.76	51.86	51.23	1
GRB110106B	0.618	43.42	20.50	2.06	51.44	50.01	1
GRB101219B	0.55185	41.86	25.90	1.67	51.45	50.02	1
GRB101213A	0.414	131.12	49.90	2.27	51.50	49.53	1
GRB100906A	1.727	114.63	119.00	10.02	52.98	51.35	1
GRB100902A	4.5	428.83	32.20	0.96	52.97	51.07	4
GRB100901A	1.4084	436.66	19.50	0.79	52.05	49.79	1
GRB100814A	1.44	177.26	88.50	2.47	52.73	50.86	1
GRB100728B	2.106	12.08	16.70	3.47	52.25	51.66	1
GRB100728A	1.567	193.38	373.00	5.00	53.41	51.53	1
GRB100704A	3.6	196.88	58.50	4.30	53.11	51.48	4
GRB100621A	0.542	63.55	206.00	12.61	52.34	50.72	1
GRB100615A	1.398	38.82	49.20	5.56	52.45	51.24	1
GRB100513A	4.772	83.50	14.30	0.57	52.64	51.48	1
GRB100508A	0.5201	49.26	7.50	0.47	50.86	49.35	1
GRB100425A	1.755	38.97	4.64	1.37	51.58	50.43	1
GRB100424A	2.465	104.00	15.00	0.33	52.30	50.83	1
GRB100418A	0.6239	7.93	3.46	1.04	50.68	49.99	1
GRB100413A	3.9	192.64	61.80	0.64	53.18	51.58	4
GRB100316B	1.18	3.84	1.98	1.34	50.93	50.69	1
GRB100316A	3.155	6.75	8.22	2.26	52.19	51.98	1
GRB100302A	4.813	17.95	3.16	0.47	51.99	51.50	1
GRB100219A	4.66723	27.57	4.65	0.40	52.14	51.46	1
GRB100213B	0.604	91.86	12.20	0.80	51.20	49.44	1
GRB091208B	1.0633	14.80	32.00	14.62	52.06	51.21	1
GRB091127	0.49044	6.96	85.80	45.31	51.87	51.20	1
GRB091109A	3.076	48.03	16.40	1.23	52.47	51.40	1
GRB091029	2.752	39.18	24.10	1.72	52.58	51.56	1
GRB091024	1.092	112.28	59.80	2.06	52.35	50.62	1
GRB091020	1.71	38.92	38.00	4.18	52.48	51.32	1
GRB091018	0.971	4.37	15.20	10.38	51.67	51.33	1
GRB090927	1.37	2.16	1.98	1.90	51.04	51.08	1
GRB090926B	1.24	99.28	71.20	3.16	52.52	50.88	1
GRB090814A	0.696	78.06	12.50	0.54	51.32	49.66	1

Table 1—Continued

GRB	z	T_{90} (s)	S (10^{-7} erg cm $^{-2}$)	P (ph s $^{-1}$ cm $^{-2}$)	$\log(E_{\text{iso}})$ (erg)	$\log(L_{\text{iso}})$ (erg s $^{-1}$)	Refs.
GRB090812	2.452	74.50	57.30	3.55	52.88	51.55	1
GRB090809A	2.737	8.87	3.65	1.08	51.75	51.38	1
GRB090726	2.71	56.68	7.86	0.79	52.08	50.90	1
GRB090715B	3	266.40	56.50	3.75	52.99	51.17	1
GRB090709A	1.8	88.74	253.00	7.79	53.33	51.83	1
GRB090618	0.54	113.34	1090.00	1.73	53.06	51.19	1
GRB090530	1.266	40.46	10.90	3.19	51.72	50.47	1
GRB090529A	2.625	70.44	10.40	0.69	52.18	50.89	1
GRB090519	3.85	58.04	11.80	0.57	52.45	51.37	1
GRB090516A	4.109	181.01	92.10	2.31	53.38	51.83	1
GRB090429B	9.38	5.58	3.29	1.63	52.30	52.57	1
GRB090424	0.544	49.46	218.00	69.92	52.36	50.86	1
GRB090423	8.26	10.30	6.24	1.74	52.53	52.48	1
GRB090418A	1.608	56.30	46.60	1.90	52.52	51.19	1
GRB090407	1.4485	315.47	11.40	0.66	51.84	49.73	1
GRB090404	2.87	82.02	31.20	1.97	52.71	51.39	1
GRB090313	3.3736	83.04	15.10	0.75	52.49	51.21	1
GRB090205	4.6497	8.81	2.03	0.48	51.78	51.59	1
GRB090201	2.1	74.26	289.00	14.57	53.49	52.11	1
GRB090113	1.7493	9.10	7.75	2.47	51.80	51.28	1
GRB090102	1.547	28.32	70.60	0.21	52.68	51.63	1
GRB081230	2.03	60.69	8.59	0.71	51.94	50.64	1
GRB081228	3.44	3.00	0.93	0.62	51.29	51.46	1
GRB081222	2.77	33.00	52.20	7.46	52.91	51.97	1
GRB081221	2.26	33.91	189.00	17.95	53.35	52.33	1
GRB081210	2.0631	145.91	18.50	2.45	52.29	50.61	2
GRB081203A	2.05	223.00	78.30	2.82	52.91	51.04	1
GRB081121	2.512	17.52	50.80	4.15	52.85	52.15	1
GRB081118	2.58	53.40	11.80	0.60	52.23	51.05	1
GRB081109A	0.9787	221.49	40.00	1.41	52.10	50.05	1
GRB081029	3.8479	275.10	21.40	0.45	52.71	50.95	1
GRB081028A	3.038	284.42	39.50	0.57	52.85	51.00	1
GRB081008	1.9683	187.82	42.50	1.29	52.62	50.82	1
GRB081007	0.5295	9.73	7.61	2.87	50.89	50.08	1
GRB080928	1.6919	233.66	24.30	2.08	52.27	50.34	1
GRB080916A	0.6887	61.35	42.20	2.62	51.84	50.28	1
GRB080913	6.733	7.46	5.72	1.37	52.40	52.42	1
GRB080906	2.13	148.21	36.50	1.02	52.60	50.93	1
GRB080905B	2.3739	120.94	18.10	1.62	52.36	50.81	1
GRB080810	3.3604	107.67	46.40	1.98	52.97	51.58	1
GRB080805	1.5042	106.62	26.50	1.04	52.23	50.60	1
GRB080804	2.2045	37.87	37.90	3.06	52.64	51.57	1
GRB080721	2.5914	129.70	155.00	0.71	53.35	51.79	1
GRB080710	0.8454	142.99	15.30	0.92	51.57	49.68	1
GRB080707	1.2322	30.16	6.26	1.06	51.46	50.33	1

Table 1—Continued

GRB	z	T_{90} (s)	S (10^{-7} erg cm^{-2})	P ($\text{ph s}^{-1} \text{cm}^{-2}$)	$\log(E_{\text{iso}})$ (erg)	$\log(L_{\text{iso}})$ (erg s^{-1})	Refs.
GRB080607	3.0368	78.97	247.00	23.30	53.64	52.35	1
GRB080605	1.6403	18.06	134.00	0.94	53.00	52.16	1
GRB080604	1.4171	77.61	7.89	0.38	51.66	50.16	1
GRB080603B	2.6892	59.12	24.60	3.53	52.57	51.37	1
GRB080602	1.8204	74.29	32.60	2.73	52.45	51.03	1
GRB080520	1.5457	3.32	0.59	0.49	50.60	50.48	1
GRB080517	0.089	64.51	5.87	0.60	49.24	47.47	1
GRB080516	3.2	5.76	2.67	1.70	51.71	51.57	1
GRB080515	2.47	20.86	25.80	3.42	52.54	51.76	1
GRB080430	0.767	13.87	11.70	2.66	51.37	50.48	1
GRB080413B	1.1014	8.00	33.60	18.13	52.11	51.53	1
GRB080413A	2.433	46.36	35.20	5.52	52.67	51.54	1
GRB080411	1.0301	56.33	265.00	40.61	52.96	51.51	1
GRB080330	1.5119	60.36	2.94	0.94	51.28	49.90	1
GRB080325	1.78	166.74	50.10	1.43	52.62	50.84	1
GRB080319C	1.9492	29.55	35.10	5.09	52.53	51.53	1
GRB080319B	0.9382	124.86	855.00	1.24	53.39	51.59	1
GRB080319A	2.0265	43.62	44.50	2.60	52.66	51.50	2
GRB080310	2.42743	363.21	23.10	1.32	52.48	50.46	1
GRB080210	2.6419	42.26	18.00	1.59	52.42	51.36	1
GRB080207	2.0858	292.46	64.00	1.10	52.83	50.85	1
GRB080205	2.72	106.30	20.30	1.40	52.49	51.04	2
GRB080129	4.349	50.18	8.39	0.55	52.36	51.39	1
GRB071122	1.14	71.43	6.16	0.41	51.40	49.88	1
GRB071117	1.3308	6.08	24.20	0.42	52.11	51.69	1
GRB071031	2.6918	180.64	8.98	0.54	52.13	50.44	1
GRB071025	5.2	241.30	73.20	1.71	53.39	51.80	1
GRB071021	2.452	228.72	13.60	0.63	52.26	50.44	1
GRB071020	2.1462	4.30	23.40	0.61	52.41	52.28	1
GRB071010B	0.947	36.12	46.20	7.37	52.13	50.87	1
GRB071010A	0.985	6.32	2.02	0.89	50.81	50.30	1
GRB071003	1.60435	148.39	83.50	6.35	52.77	51.02	1
GRB070810A	2.17	9.04	6.72	1.89	51.88	51.42	1
GRB070808	1.35	58.43	12.90	1.94	51.84	50.45	2
GRB070802	2.4541	15.80	2.79	0.45	51.57	50.91	1
GRB070721B	3.6298	336.86	35.60	1.56	52.90	51.04	1
GRB070714A	1.58	3.00	1.55	1.90	51.03	50.97	1
GRB070612A	0.617	365.28	108.00	1.37	52.16	49.81	1
GRB070611	2.0394	13.18	4.03	0.80	51.62	50.98	1
GRB070529	2.4996	108.90	24.80	1.46	52.53	51.04	1
GRB070521	2.0865	38.63	82.10	0.40	52.94	51.84	1
GRB070518	1.16	5.50	1.67	0.67	50.85	50.44	1
GRB070508	0.82	20.90	201.00	24.25	52.66	51.60	1
GRB070506	2.309	5.99	2.30	0.99	51.45	51.19	1
GRB070420	3.01	77.02	142.00	7.06	53.40	52.11	1

Table 1—Continued

GRB	z	T_{90} (s)	S (10^{-7} erg cm $^{-2}$)	P (ph s $^{-1}$ cm $^{-2}$)	$\log(E_{\text{iso}})$ (erg)	$\log(L_{\text{iso}})$ (erg s $^{-1}$)	Refs.
GRB070419B	1.9588	238.01	74.40	1.36	52.86	50.95	1
GRB070419A	0.9705	160.00	6.67	0.06	51.31	49.40	1
GRB070411	2.9538	115.69	26.90	0.93	52.66	51.20	1
GRB070328	2.06	72.12	91.50	4.21	52.98	51.61	1
GRB070318	0.8397	130.37	26.20	1.61	51.80	49.94	1
GRB070306	1.49594	209.24	54.60	4.06	52.54	50.62	1
GRB070224	1.99	48.00	3.70	0.20	51.56	50.36	1
GRB070223	1.6295	128.00	17.90	0.44	52.12	50.43	2
GRB070208	1.165	64.00	5.18	0.38	51.34	49.87	1
GRB070129	2.3384	459.75	30.00	0.56	52.57	50.43	1
GRB070110	2.3521	88.43	16.30	0.61	52.31	50.89	1
GRB070103	2.6208	18.41	3.29	1.05	51.68	50.98	1
GRB061222B	3.355	37.25	22.70	1.50	52.66	51.73	1
GRB061222A	2.088	100.00	85.10	7.45	52.96	51.45	1
GRB061202	2.2543	94.19	34.50	2.47	52.61	51.15	2
GRB061126	1.1588	52.62	66.50	0.46	52.45	51.06	1
GRB061121	1.3145	81.22	139.00	1.00	52.86	51.31	1
GRB061110B	3.4344	135.25	13.50	0.46	52.45	50.96	1
GRB061110A	0.7578	44.51	11.30	0.47	51.35	49.95	1
GRB061021	0.3463	47.82	30.10	6.12	51.12	49.57	1
GRB061007	1.2622	75.74	450.00	0.96	53.34	51.81	1
GRB060927	5.4636	22.42	11.20	2.68	52.60	52.06	1
GRB060926	3.2086	8.82	2.32	1.10	51.65	51.32	1
GRB060923B	1.51	8.95	4.90	1.42	51.50	50.95	1
GRB060923A	2.47	58.49	9.77	1.37	52.12	50.89	1
GRB060912A	0.937	5.03	13.60	8.54	51.60	51.18	1
GRB060908	1.8836	19.30	28.10	2.98	52.41	51.58	1
GRB060906	3.6856	44.59	22.90	1.98	52.72	51.74	1
GRB060904B	0.7029	189.98	17.10	2.43	51.47	49.42	1
GRB060904A	2.55	80.06	78.30	4.91	53.04	51.69	1
GRB060814	1.9229	145.07	148.00	7.31	53.14	51.45	1
GRB060805A	2.3633	4.93	0.73	0.31	50.97	50.80	1
GRB060729	0.5428	113.04	26.10	1.15	51.44	49.58	1
GRB060719	1.532	66.92	15.30	2.15	52.01	50.58	1
GRB060714	2.7108	116.06	28.80	1.27	52.64	51.15	1
GRB060708	1.92	10.03	4.99	1.91	51.67	51.13	1
GRB060707	3.424	66.64	15.80	1.08	52.51	51.34	1
GRB060614	0.1254	109.10	188.00	11.49	51.04	49.05	1
GRB060607A	3.0749	103.03	25.70	1.40	52.67	51.26	1
GRB060605	3.773	79.84	7.11	0.47	52.22	51.00	1
GRB060604	2.1357	96.00	3.76	0.02	51.62	50.13	1
GRB060602A	0.787	74.84	16.10	0.56	51.53	49.91	1
GRB060526	3.2213	298.04	12.90	1.67	52.39	50.54	1
GRB060522	5.11	69.12	11.30	0.54	52.57	51.52	1
GRB060512	2.1	8.40	2.31	0.89	51.39	50.96	1

Table 1—Continued

GRB	z	T_{90} (s)	S (10^{-7} erg cm $^{-2}$)	P (ph s $^{-1}$ cm $^{-2}$)	$\log(E_{\text{iso}})$ (erg)	$\log(L_{\text{iso}})$ (erg s $^{-1}$)	Refs.
GRB060510B	4.941	262.94	39.80	0.57	53.10	51.46	1
GRB060502A	1.5026	28.45	23.30	1.73	52.18	51.12	1
GRB060428B	0.348	96.00	8.44	0.31	50.58	48.72	1
GRB060418	1.49	109.08	84.00	6.56	52.73	51.08	1
GRB060319	1.172	10.29	2.65	1.07	51.05	50.38	1
GRB060306	1.559	60.94	21.50	5.92	52.17	50.79	1
GRB060223A	4.41	11.32	6.74	1.35	52.28	51.96	1
GRB060210	3.9122	288.00	76.80	1.20	53.27	51.50	1
GRB060206	4.0559	7.55	8.42	2.78	52.33	52.16	1
GRB060204B	2.3393	139.46	29.30	1.33	52.56	50.94	2
GRB060202	0.783	192.88	22.20	0.53	51.67	49.63	1
GRB060124	2.3	13.42	4.65	0.86	51.75	51.14	1
GRB060117	4.6	16.85	210.00	48.49	53.79	53.31	1
GRB060116	6.6	104.83	23.90	1.17	53.02	51.88	1
GRB060115	3.5328	139.09	17.10	0.86	52.57	51.08	1
GRB060111A	2.32	13.21	12.00	1.71	52.17	51.57	1
GRB060108	2.03	14.22	3.72	0.75	51.58	50.91	1
GRB051117B	0.481	9.02	1.75	0.50	50.17	49.38	1
GRB051111	1.54948	64.00	42.70	1.83	52.46	51.06	1
GRB051109B	0.08	15.70	2.65	0.57	48.80	47.64	1
GRB051109A	2.346	37.20	21.70	3.88	52.43	51.39	1
GRB051016B	0.9364	4.00	1.67	1.29	50.68	50.37	1
GRB051008	2.77	12.41	50.80	0.19	52.90	52.39	1
GRB051006	1.059	35.41	13.50	1.68	51.69	50.45	1
GRB051001	2.4296	190.26	17.60	0.48	52.37	50.62	1
GRB050922C	2.1995	4.55	16.20	7.09	52.27	52.12	1
GRB050922B	4.5	157.02	23.70	1.09	52.83	51.38	1
GRB050915A	2.5273	53.42	8.36	0.76	52.07	50.89	1
GRB050908	3.3467	18.28	4.83	0.70	51.99	51.36	1
GRB050904	6.295	181.58	52.10	0.63	53.33	51.94	1
GRB050826	0.296	29.60	4.20	0.37	50.13	48.78	1
GRB050824	0.8278	25.01	2.78	0.48	50.81	49.67	1
GRB050822	1.434	104.29	25.10	2.23	52.18	50.54	1
GRB050820A	2.6147	240.77	38.30	2.44	52.75	50.92	1
GRB050819	2.5043	37.72	3.48	0.40	51.68	50.65	1
GRB050814	5.3	142.85	19.10	0.67	52.82	51.46	1
GRB050803	3.5	88.12	21.60	0.96	52.66	51.37	1
GRB050802	1.7102	27.46	22.10	2.66	52.24	51.23	1
GRB050801	1.38	19.57	3.09	1.47	51.24	50.32	1
GRB050730	3.9693	154.60	23.60	0.56	52.77	51.27	1
GRB050726	0.1646	46.50	19.60	1.37	50.30	48.70	1
GRB050714B	2.438	49.36	6.30	0.55	51.92	50.76	1
GRB050603	2.821	21.00	82.10	0.76	53.12	52.38	1
GRB050525A	0.606	8.84	151.00	43.85	52.29	51.55	1
GRB050505	4.2748	58.85	24.90	1.84	52.83	51.78	1

Table 1—Continued

GRB	z	T_{90} (s)	S (10^{-7} erg cm $^{-2}$)	P (ph s $^{-1}$ cm $^{-2}$)	$\log(E_{\text{iso}})$ (erg)	$\log(L_{\text{iso}})$ (erg s $^{-1}$)	Refs.
GRB050502B	5.2	17.72	4.72	1.39	52.20	51.75	1
GRB050416A	0.6528	6.67	4.13	4.86	50.79	50.19	1
GRB050406	2.7	5.78	0.78	0.34	51.07	50.88	1
GRB050401	2.8983	32.09	80.90	12.17	53.13	52.22	1
GRB050319	3.2425	151.58	13.30	1.46	52.41	50.86	1
GRB050318	1.4436	16.12	10.40	3.13	51.80	50.98	1
GRB050315	1.95	95.40	31.70	1.89	52.48	50.97	1
GRB050223	0.584	22.68	6.48	0.65	50.90	49.74	1
GRB050219A	0.2115	23.81	40.80	3.43	50.83	49.54	1
GRB050215B	2.52	11.04	2.35	0.67	51.51	51.02	1
GRB050126	1.29	48.00	8.85	0.31	51.65	50.33	1

Note. — We give the name, redshift z , duration T_{90} , fluence S in 15-150 keV, peak photon flux P , isotropic energy E_{iso} , and luminosity L_{iso} . E_{iso} and L_{iso} are estimated in the 45-450 keV energy range. Redshifts are provided in following references: (1) Lien et al. (2016); (2) Perley et al. (2016a); (3) Greiner’s online GRB table; (4) the Swift GRB table: http://swift.gsfc.nasa.gov/archive/grb_table.html/.

Table 2. Table of LGRB Hosts

GRB	z	$\log(Z/Z_{\odot})$	Ref.
GRB131231A	0.6427	-0.24	1
GRB131103A	0.596	-0.21	1
GRB130925A	0.3483	0.04	1, 3
GRB130702	0.145	-0.5	3
GRB130603B	0.3568	-0.25	3
GRB130427A	0.3401	-0.12	1, 3
GRB120722A	0.959	-0.21	1
GRB120714B	0.3985	-0.3	1
GRB120422A	0.2826	-0.3	1
GRB111209A	0.677	-0.74	1, 3
GRB110918A	0.9843	0.24	1, 3
GRB100816A	0.8048	0.06	1
GRB100621A	0.5426	-0.17	1, 2
GRB100508A	0.5201	-0.01	1
GRB100418A	0.6235	-0.17	1, 3
GRB100206	0.4068	0.51	3
GRB091127	0.4903	-0.29	1, 2, 3
GRB091018	0.971	0.09	1, 2
GRB090424	0.5445	0.19	2, 3
GRB081109	0.9785	0.06	1
GRB081007	0.5294	-0.37	2
GRB080916A	0.688	-0.25	2
GRB080430	0.767	-1.09	2
GRB071227	0.381	-0.2	3
GRB071112C	0.821	-0.79	2
GRB070612	0.671	-0.4	3
GRB061021	0.3453	-0.21	2
GRB060912A	0.9362	-0.08	1, 2
GRB060614A	0.125	-0.23	2
GRB060505	0.0889	-0.22	3
GRB051117B	0.4805	0.31	1
GRB051022A	0.8061	-0.2	1, 3
GRB051016B	0.9358	-0.42	1
GRB050826	0.296	0.14	3
GRB050824	0.8277	-0.58	1
GRB050416A	0.6542	-0.23	1, 2
GRB031203	0.1055	-0.64	3
GRB020405	0.691	-0.2	3
GRB010921	0.451	-0.6	3
GRB991208	0.706	-0.67	3
GRB980703	0.966	-0.2	3
GRB980425	0.0085	-0.5	3

References. — (1) Krühler et al. (2015); (2) Japelj et al. (2016); (3) GHostS